JGR Oceans

RESEARCH ARTICLE
10.1029/2021JC018115

Transports and Pathways of the Tropical AMOC Return Flow From Argo Data and Shipboard Velocity Measurements

Franz Philip Tuchen[1,2], Peter Brandt[1,3], Joke F. Lübbecke[1,3], and Rebecca Hummels[1]

[1]GEOMAR Helmholtz Centre for Ocean Research Kiel, Kiel, Germany, [2]Now at NOAA/Atlantic Oceanographic and Meteorological Laboratory, Miami, FL, USA, [3]Faculty of Mathematics and Natural Sciences, Kiel University, Kiel, Germany

Abstract The upper-ocean circulation of the tropical Atlantic is a complex superposition of thermohaline and wind-driven flow components. The resulting zonally and vertically integrated upper-ocean meridional flow is referred to as the upper branch of the Atlantic Meridional Overturning Circulation (AMOC)—a major component and potential tipping element of the global climate system. Here, we investigate the tropical part of the northward AMOC branch, that is, the return flow covering the upper 1,200 m, based on Argo data and repeated shipboard velocity measurements. The western boundary mean circulation at 11°S is realistically reproduced from high-resolution Argo data showing a remarkably good representation of the volume transport of the return flow water mass layers when compared to results from direct velocity measurements along a repeated ship section. The AMOC return flow through the inner tropics (11°S–10°N) is found to be associated with a diapycnal upwelling of lower central water into the thermocline layer of ∼2 Sv. This is less than half the magnitude of previous estimates, likely due to improved horizontal resolution. The total AMOC return flow at 11°S and 10°N is derived to be similar in strength with 16–17 Sv. At 11°S, northward transport is concentrated at the western boundary, where the AMOC return flow enters the inner tropics at all vertical levels above 1,200 m. At 10°N, northward transport is observed both at the western boundary and in the interior predominantly in the surface and intermediate layer indicating recirculation and transformation of thermocline and lower central water within the inner tropics.

Plain Language Summary The Atlantic Meridional Overturning Circulation (AMOC) is one of the major components of the global climate system. In the upper 1,200 m, the northward branch of the AMOC transports large amounts of heat, salt, and biogeochemical tracers across the equator from the South Atlantic through the tropics to the North Atlantic. In this study, we show that a realistic reconstruction of the upper-ocean circulation at the southern hemisphere western boundary—a bottleneck for the AMOC—is possible based on high-resolution Argo float data, further enabling transport and pathway estimates for the upper and intermediate water mass layers of the inner tropical Atlantic (11°S–10°N). At 11°S, the northward AMOC branch is largely concentrated at the western boundary, whereas, at 10°N, it preferably exits the inner tropics through the western boundary, but also through the interior basin after recirculating in the equatorial current system. When crossing the inner tropics, the water masses forming the AMOC return flow change their characteristics and the associated upwelling of water into the subsurface layer is found here to be less than half as large as previously estimated, likely due to improved horizontal resolution.

Key Points:

- Observed Atlantic western boundary mean transport of the upper 1,200 m at 11°S is realistically reproduced from high-resolution Argo data
- Diapycnal transport estimates from high-resolution Argo data show upwelling of ∼2 Sv into the tropical Atlantic thermocline layer
- By combining shipboard measurements with Argo data, we provide an overview of the individual water mass pathways within the Atlantic Meridional Overturning Circulation return flow

Supporting Information:

Supporting Information may be found in the online version of this article.

Correspondence to:

F. P. Tuchen,
ftuchen@geomar.de;
franz.philip.tuchen@noaa.gov

Citation:

Tuchen, F. P., Brandt, P., Lübbecke, J. F., & Hummels, R. (2022). Transports and pathways of the tropical AMOC return flow from argo data and shipboard velocity measurements. *Journal of Geophysical Research: Oceans*, *127*, e2021JC018115. https://doi.org/10.1029/2021JC018115

Received 8 OCT 2021
Accepted 14 JAN 2022

1. Introduction

The mean climate in the North Atlantic region is largely impacted by the presence of one of the major components of the global climate system: the Atlantic Meridional Overturning Circulation (AMOC; e.g., Rahmstorf, 2002). In a zonally averaged view, the circulation pattern associated with the AMOC can be divided into a shallow northward branch, a deep southward branch (North Atlantic Deep Water; NADW), and another northward branch close to the ocean floor consisting of Antarctic Bottom Water (AABW) which are best described as the vertically integrated meridional transport across a certain latitude including thermohaline and wind-driven transport components. Within the shallow branch of the AMOC, that is, the return flow in the upper ∼1,200 m, large amounts of heat, salt, and biogeochemical tracers (e.g., oxygen or carbon) are transported from the South Atlantic through the tropics to the subpolar North Atlantic and Arctic Ocean where the conversion of warm and salty water into colder and fresher deep waters constitutes the downward limb of the overturning circulation (Johns et al., 2011; Lozier et al., 2019; Zhang & Thomas, 2021). One likely consequence of global warming is a decline of the meridional volume transport associated with the AMOC (e.g., Hoegh-Guldberg et al., 2018), although the strength of this

decline is still under vigorous scientific debate. Therefore, the AMOC is considered a potential tipping element of the Earth's future climate (e.g., Lenton et al., 2008).

Direct measurements of the AMOC strength at different locations throughout the Atlantic Ocean have not been able to provide evidence of such a global warming-induced weakening during the observational period covering the last 20–30 years (Fu et al., 2020; Moat et al., 2020; Worthington et al., 2021). It is believed that multidecadal variability in combination with comparably short observational time series complicates the detection of possible long-term AMOC trends. Nevertheless, recently, Caesar et al. (2021) inferred a rapid AMOC weakening since the mid-20th century from various proxy indicators. In another recent study by Boers (2021) it is suggested that the AMOC decline argued by Caesar et al. (2021) could be an indication of the AMOC transitioning into a weak circulation mode further fueling the ongoing debate about observed trends, long-term variations and internal variability of the AMOC.

For the last two decades, several international efforts have established continuous measurements of the different AMOC components (Frajka-Williams et al., 2019) with trans-basin mooring arrays at selected latitudes in the subpolar (OSNAP; Lozier et al., 2019) and in the subtropical North (RAPID-MOCHA; Cunningham et al., 2007) and South Atlantic (SAMBA; Meinen et al., 2018). More confined mooring arrays are used to monitor the deep southward branch in the subtropical (Line W from 2004 to 2014; Toole et al., 2017) and tropical North Atlantic (16°N/MOVE; Send et al., 2011) or the deep western boundary current (DWBC) and the North Brazil Undercurrent (NBUC) in the tropical South Atlantic (11°S/TRACOS; Herrford et al., 2021; Hummels et al., 2015; Schott et al., 2005). Due to the discrete nature of mooring arrays, a coherent picture of the AMOC pathways has been generally limited to model simulations (e.g., Bower et al., 2019; Rühs et al., 2019; Speich et al., 2001) and to schematic views based on limited direct observations (Schott et al., 1998; Stramma & England, 1999; Stramma & Schott, 1999).

One promising advancement for the global hydrographic data coverage is the continuing effort of the Argo program (Argo, 2000). With a concurrent operation of about 4,000 floats, each providing one hydrographic profile of the upper 2,000 m every 10 days (Wong et al., 2020), the accumulated data has reached a point where the prospects and limitations of reconstructing the large-scale upper-ocean geostrophic mean circulation deserve further attention. Previous studies already demonstrated that by assimilating Argo data in model simulations the representation of the AMOC and, for instance, its associated heat transport is greatly improved (e.g., Dong et al., 2011). In this study, we explore the ability of Argo float data to reproduce the observed mean upper-ocean circulation in a case study for the western boundary circulation at 11°S, where, in addition to the moored velocity array, repeated ship sections of current velocity have been collected over the last 20 years providing a reliable reference (Hummels et al., 2015; Schott et al., 2005).

The western boundary circulation at 11°S is a complex and depth-dependent superposition of contributions from (a) the thermohaline circulation (THC) and (b) the wind-driven shallow overturning circulations, known as the Subtropical Cells (STCs), as well as of (c) the western boundary compensation of the interior ocean Sverdrup balance (Schott et al., 2005). In particular, the equatorward NBUC at the western boundary of the tropical South Atlantic, which is the dominant pathway for the AMOC return flow at these latitudes, is composed of all three transport components at thermocline level (da Silveira et al., 1994; Hummels et al., 2015; Stramma et al., 1995).

In a zonal average, the STCs consist of poleward Ekman transport in the surface layer, subduction of water in the subtropics, equatorward geostrophic flow at thermocline level and equatorial and eastern boundary upwelling (Figure 1). The superposition of the THC on the STC circulation is known to cause an interhemispheric asymmetry in equatorward thermocline layer transports (see Figure 1) in which the southern hemisphere STC is strengthened and the northern hemisphere STC circulation is weakened (e.g., Fratantoni et al., 2000; Hazeleger & Drijfhout, 2006; Schott et al., 2004). Consequently, changes of the Atlantic THC are expected to have implications for the upper-ocean heat content and freshwater distribution by impacting the observed asymmetry of the STCs (Chang et al., 2008). Variations in the STC strength are suggested to modulate sea surface temperature on decadal time scales (Rabe et al., 2008, Tuchen et al., 2020) as well as to contribute to long-term transport variance of the equatorial zonal current system. For the tropical thermocline, the STCs represent an important ventilation mechanism (Luyten et al., 1983) with consequences for the lateral oxygen ventilation (Brandt et al., 2021).

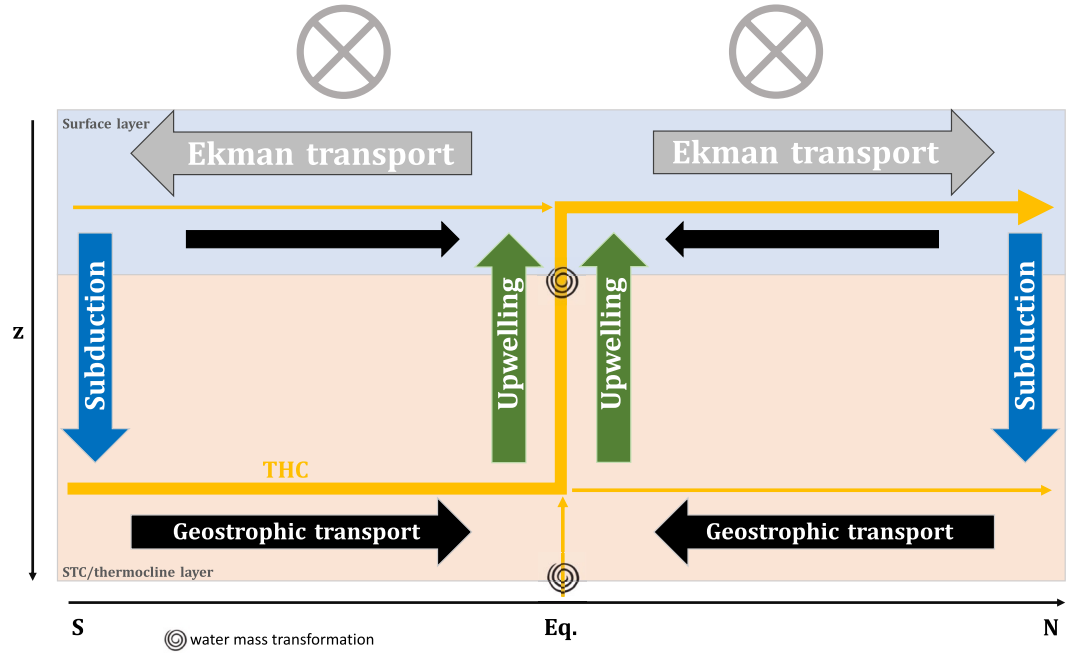

Figure 1. Schematic of the zonally averaged circulation of the upper-ocean tropical Atlantic highlighting the superposition of the wind-driven Subtropical Cells (STCs) and the northward branch of the thermohaline circulation (THC). Easterly trade winds at the ocean surface (gray crosses) induce poleward Ekman transport (gray arrows) within the surface layer (blue shaded). At subtropical latitudes, water is subducted (blue arrows) into the STC/thermocline layer (beige shaded) and transported back to the tropics following geostrophic contours (black arrows). The STCs are closed by equatorial and eastern boundary upwelling (green arrows). Note that the surface layer also experiences equatorward geostrophic transport (black arrows) partly compensating the Ekman transport. The THC with its partial tropical upwelling into the STC/thermocline layer and into the surface layer is indicated schematically by the yellow arrows; water mass transformation associated with diapycnal transports by black whirls.

Estimates of the STC strength are often carried out along 10°N and 10°S due to the presence of shallower overturning cells (i.e., the tropical cells) closer to the equator (e.g., Molinari et al., 2003; Perez et al., 2014) and due to the bifurcation of the westward branches of the subtropical gyres further poleward (e.g., Schott et al., 2004; Tuchen et al., 2019). Therefore, water entering the STC/thermocline layer equatorward of these latitudes through diapycnal transport from deeper levels, as part of the overall tropical upwelling of the AMOC return flow (see Figure 1), has been estimated as the residual of horizontal transport divergence/convergence in the surface layer and STC/thermocline layer (e.g., Tuchen et al., 2019; Zhang et al., 2003). Hence, STC transport uncertainties, which especially arise at the western boundary where observations are rather sparse, can project onto this residual and lead to upwelling estimates with large uncertainties (Tuchen et al., 2019). Observational estimates of the overall tropical upwelling associated with the AMOC return flow are rare since they require closed zonal trans-Atlantic sections in order to calculate the transformation rates of the individual water mass layers (e.g., Lux et al., 2001; Roemmich, 1983). Roemmich (1983) estimated a diapycnal upwelling of 6 Sv (1 Sv = $10^6 m^3 s^{-1}$) into the STC/thermocline layer from two zonal ship sections carried out in the 1950s along 8°N/S, whereas Lux et al. (2001) even estimated a downwelling from the thermocline layer into the lower layers. Clearly, an accurate description of the STCs depends on the accuracy of the upwelling of the AMOC return flow when crossing the tropics. Therefore, one aim of this study is to quantify the diapycnal mean transport of lower central water into the STC/thermocline layer with high-resolution Argo data and to compare it with previous estimates.

This study is organized as follows: Section 2 provides an overview of the used data sets. In Section 3, the methods to derive the individual transport components are described. In Section 4, Argo-derived western boundary transports are compared to and validated by transports from a repeated ship section at the western boundary along 11°S. Building up on the realism of the reconstructed transports, we derive an estimate of the tropical diapycnal transports between the individual layers that participate in the AMOC return flow in Section 5. Section 6 provides an overview of the mean transports and pathways of the AMOC return flow derived from a combination of Argo

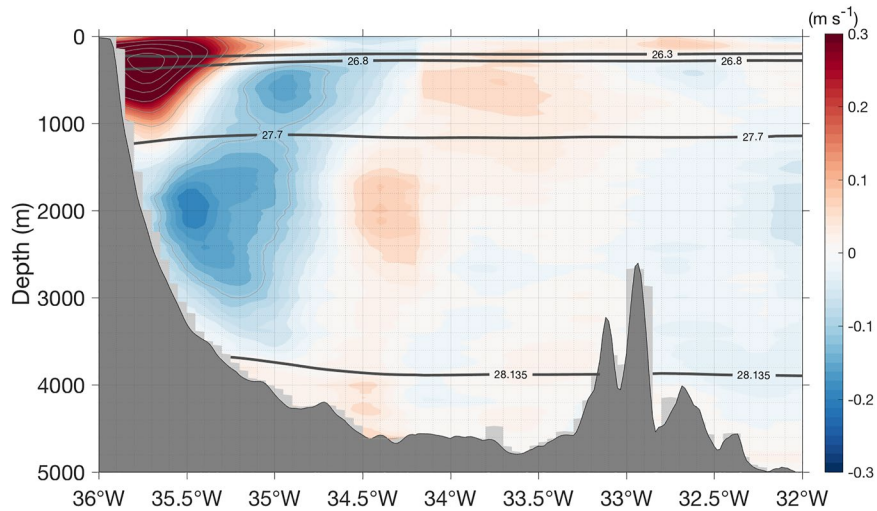

Figure 2. Mean meridional (east of 34.2°W) and alongshore (west of 34.2°W, rotated clockwise by 36°) velocity at 11°S from 12 individual acoustic Doppler current profiler sections (2000–2019). Solid thick lines represent neutral density surfaces and separate the different water masses according to Table 1. The gray solid lines mark intervals of 0.1 ms^{-1}.

float data, satellite wind speed data and current velocity data from additional ship sections along 5°S, 35°W, and 23°W. The presented results are discussed in Section 7 followed by our conclusions in Section 8.

2. Data

Hydrographic profiles from Argo floats are provided by the Roemmich & Gilson Argo climatology (Roemmich & Gilson, 2009) as gridded means with a horizontal resolution of either 1/6° (hereafter called ARGO-HR) or 1° (hereafter, called ARGO-LR) both including Argo float observations from 2004 to 2018. A detailed description of the ARGO-LR climatology is given by Roemmich and Gilson (2009) and updated versions are regularly provided. The ARGO-HR mean is based on a weighted least squares fit to the nearest 33 Argo profiles (instead of the nearest 100 Argo profiles as for the monthly resolved ARGO-LR climatology). ARGO-LR has already been used to estimate parts of the Atlantic STC mean circulation (Tuchen et al., 2019) and STC transport variability (Tuchen et al., 2020) also pointing to limitations at the western boundary when compared to ship-based and moored velocity data at 11°S. ARGO-HR has been used in combination with expendable bathythermograph (XBT) profiles and moored velocity data to reconstruct the East Australian Current (Zilberman et al., 2018). Here, we use an updated version of the ARGO-HR product used in Zilberman et al. (2018), and compare it to ship section data taken at the Atlantic Ocean western boundary at 11°S. These data include a total of 12 individual ship sections with a reasonable coverage of the different seasons (see Figure S1 in Supporting Information S1) in order to derive a representative mean section of meridional/along-shore velocity (Figure 2). A more detailed description of the velocity data is provided by Schott et al. (2005) covering the measurements between 2000 and 2004 and by Hummels et al. (2015) for the ongoing resumption of the measurements since 2013.

The shipboard velocity sections at 11°S are derived from a weighted combination of full-depth lowered acoustic Doppler current profiler (LADCP) data at discrete stations and two simultaneously operating vessel-mounted ADCPs (vmADCP) with a frequency of 38 and 75 kHz, respectively, for the upper part of the water column. Additional mean ship section data at 5°S (15 individual sections from 1990 to 2019), 35°W (16 individual sections from 1990 to 2006) and 23°W (27 individual sections from 2000 to 2018) have been derived analogously by merging LADCP (if available) and vmADCP data. Zonal velocity data from the meridional sections along 35°W and 23°W will be used here to highlight the observed mean zonal pathways of the AMOC return flow within the tropical current system (see Figure 3 for an overview map including the location and extent of the described ship sections). Current velocities derived from shipboard measurements typically do not cover the upper 10–20 m and are often extrapolated to the surface. Here, velocities in the upper 10 m are replaced by the gridded mean surface current velocities at 1/4° horizontal resolution derived from satellite-tracked surface drifting buoys (Laurindo et al., 2017) that were horizontally interpolated to the resolution of the individual ship sections.

As described in detail in the next section, the geostrophic transport component can be inferred from hydrographic profiles provided by Argo observations. However, the wind-driven transport component in the surface layer must be accounted for separately. Here, we are using satellite-based wind speed data from the Advanced Scatterometer (ASCAT) to derive Ekman transports. ASCAT provides weekly averaged data on a horizontal grid with a resolution of 1/4° since March 2007 from which we calculated a mean wind speed field including data of the fully covered years from 2008 to 2020 (Ricciardulli & Wentz, 2016).

3. Methods

The upper-ocean circulation consists of geostrophic and wind-driven flow components which can be separately derived to approximate the total flow field. The geostrophic flow component is inferred from hydrographic data provided by Argo float observations. From vertical profiles of conservative temperature and absolute salinity, the dynamic height anomaly at each grid point is calculated from which the meridional (p_y) and zonal (p_x) gradients are used to derive the zonal (u_g) and meridional (v_g) relative geostrophic velocity component, respectively:

$$u_g = -\frac{p_y}{\rho_0 \ f} \tag{1}$$

$$v_g = \frac{p_x}{\rho_0 \ f} \tag{2}$$

Here, ρ_0 denotes a reference density (1,024 $kg\,m^{-3}$) and f the local Coriolis parameter. As a reference, we apply a level of no motion at 1,200 m which is the approximate interface between the two main branches of the AMOC (e.g., Herrford et al., 2021), separating intermediate waters from deep waters. Hydrographic data from ARGO-HR are available at each grid point down to 2,000 m. Hence, a topographic mask is applied to blank out those geostrophic velocity values at the coastal boundaries that are, unrealistically, located below the bottom depth. We have tested the sensitivity of our results to the choice of reference level and find only small changes in meridional velocity when, for instance, applying 1,000 m, 1,100 m or 1,300 m instead (Figure S2 in Supporting Information S1). Similarly, when repeating the transport calculation for ARGO-HR with reference levels varying from 1,000 m to 1,300 m, the standard error of the mean of net northward transports across 10°N (10°S) is found to be 1.7 Sv (1.0 Sv), mainly arising from uncertainties at intermediate level (not shown). In another sensitivity test, we find that the observed diapycnal transport of lower Central Water (CW) into the STC/thermocline layer between 11°S and 10°N is altered only slightly ranging from 1.4 to 2.0 Sv, when applying different reference levels of no motion for the geostrophic velocities (see Figure S3 in Supporting Information S1). The resulting mean sections of absolute meridional geostrophic velocity for both ARGO-HR and ARGO-LR along 10°N and 11°S are shown in Figure 4. Both products show a northward western boundary current which, however, is more pronounced and deeper reaching in ARGO-HR both at 11°S and 10°N (Figures 4a and 4b). At 10°N, the southward retroflection of the northward western boundary current between 55°W and 50°W is present in both means but clearly stronger in ARGO-HR (Figure 4b). It should be noted that the western boundary mean circulation at 10°N consists of a continuous northward western boundary current and the rectification of northward propagating North Brazil Current rings (NBC rings) that are shed from the retroflection (Johns et al., 1998; Schott et al., 1998).

Zonal ($T_{g,u}$) and meridional ($T_{g,v}$) geostrophic transports across meridional and zonal sections (see Figure 3) are derived by integrating the absolute geostrophic flow within vertical (z) and either zonal (x) or meridional (y) boundaries:

$$T_{g,u} = \int_{z_1}^{z_2} \int_{y_1}^{y_2} u_g \, \mathrm{d}y \, \mathrm{d}z \tag{3}$$

$$T_{g,v} = \int_{z_1}^{z_2} \int_{x_1}^{x_2} v_g \, \mathrm{d}x \, \mathrm{d}z \tag{4}$$

where, the lower vertical boundary z_2 is marked by the depth of the 27.7 $kg\,m^{-3}$ neutral density surface (γ_n) and z_1 by the surface. These boundaries define the vertical extent of the AMOC return flow including the four different water mass layers described in Table 1: surface layer, STC/thermocline layer, lower Central Water (CW) layer and Antarctic Intermediate Water (AAIW) layer. Although we generally follow the definitions for water mass

Table 1
Vertical Boundaries of the Individual Water Mass Layers Based on Neutral Density Surfaces (γ_n) or on Ekman Depth (Climatological Mean Depth at Which the Meridional Velocity Reverses Its Sign Derived From ECMWF ORA-S4; See Also Tuchen et al., 2019, e.g., at 11°S: ~60 m)

Water mass layer	Vertical boundaries (γ_n)
Surface layer	Surface to Ekman depth
STC/thermocline layer	Ekman depth to 26.3
Lower CW	26.3–26.8
AAIW	26.8–27.7
NADW	27.7–28.135
AABW	28.135–bottom

Note. Definitions are given for the surface layer, Subtropical Cell (STC)/thermocline layer, lower Central Water (CW), Antarctic Intermediate Water (AAIW), North Atlantic Deep Water (NADW) and Antarctic Bottom Water (AABW) following Hummels et al. (2015).

layers from Hummels et al. (2015), we choose to separate the surface and the STC/thermocline layer by a depth-based boundary level following Tuchen et al. (2019). This definition has no consequence for the mean transports and pathways of the overall AMOC return flow but allows us to separate the surface layer from the geostrophic STC/thermocline layer. The surface layer additionally contains a wind-driven transport component that must be accounted for separately. From wind speed data provided by the ASCAT mission (Ricciardulli & Wentz, 2016) the horizontal wind stress vector ($\vec{\tau}$) at each grid point is estimated via Bulk formula:

$$\vec{\tau} = \rho_{\text{air}}\, c_D\, \vec{u}\, |\, \vec{u}\, | \tag{5}$$

where, ρ_{air} is the density of air (1.22 $kg\,m^{-3}$), c_D is the drag coefficient (here assumed to be a constant value of 0.0013) and $\vec{u}$ the horizontal ocean surface wind speed vector. The horizontal wind stress components force the horizontal Ekman transport ($\vec{M}_e$) that is defined component-wise as:

$$M_{y,e} = -\frac{\tau_x}{\rho_0 f}$$
$$M_{x,e} = \frac{\tau_y}{\rho_0 f} \tag{6}$$

where, a zonal (meridional) wind stress excites a meridional (zonal) Ekman transport. Both Ekman and geostrophic transport estimates are functions of the Coriolis parameter that vanishes close to the equator, where, as a consequence, neither the geostrophic nor the Ekman balance holds and transport estimates largely rely on cross-equatorial shipboard observations as, for instance, along 35°W or 23°W (Figure 3) and on surface drifter data.

The derivation of diapycnal transports between 11°S and 10°N is based on the assumption of a closed volume that is laterally bounded by the South American and African coast and bounded at depth by the interface between AAIW and NADW, that is, the 27.7 $kg\,m^{-3}$ neutral density surface. Under the assumption that within these boundaries and between 11°S and 10°N volume is conserved and by accounting for a small net freshwater supply at the surface due to precipitation, evaporation and river runoff of about 0.3 Sv (Dai & Trenberth, 2003), we estimate a net divergence/convergence from the individual water mass layer transports at both sections that has to be compensated for by the layer below (see Section 5).

4. The Western Boundary Circulation at 11°S Derived From Argo Observations

In a first step, geostrophic velocity and transport data from both Argo products are compared to shipboard observations at 11°S. As previous studies have pointed to limitations of the low-resolution Argo product (ARGO-LR) at the western boundary (Tuchen et al., 2019, 2020) it is of particular interest to assess how well the high-resolution Argo product (ARGO-HR) represents well-observed circulation features. For this purpose, velocity data from a repeated ship section at the western boundary at 11°S serve as a valuable reference (Figure 2). Vertical profiles of meridional velocity are interpolated to neutral density space and vertically integrated within density bins of 0.01 $kg\,m^{-3}$ and zonally integrated within the boundaries of the ship section between the western boundary and 32°W. The resulting vertical profiles of western boundary meridional transport across 11°S from both Argo products and from ship section data are shown in Figures 5a and 5c. From ship-based current velocity data, the horizontal AMOC branches are characterized by maximum northward transports in the lower central water to intermediate water layer, depicting the shallow return flow of the AMOC within the NBUC, and by maximum southward transports in the deep-water layer associated with the DWBC. Below the DWBC, the AABW layer is associated with northward transport close to the bottom. In the following, due to the limitation of Argo float data to the upper 2,000 m of the water column, the layers below this range, that is, a large fraction of the NADW layer and the AABW layer, are not further investigated.

In comparison to the vertical profile of meridional transport from the mean ship section, the ARGO-LR transport profile shows a considerable underestimation of the transport in the northward return flow layers (Figure 5a). This discrepancy between ARGO-LR and ship-based transports at the western boundary at 11°S has already been

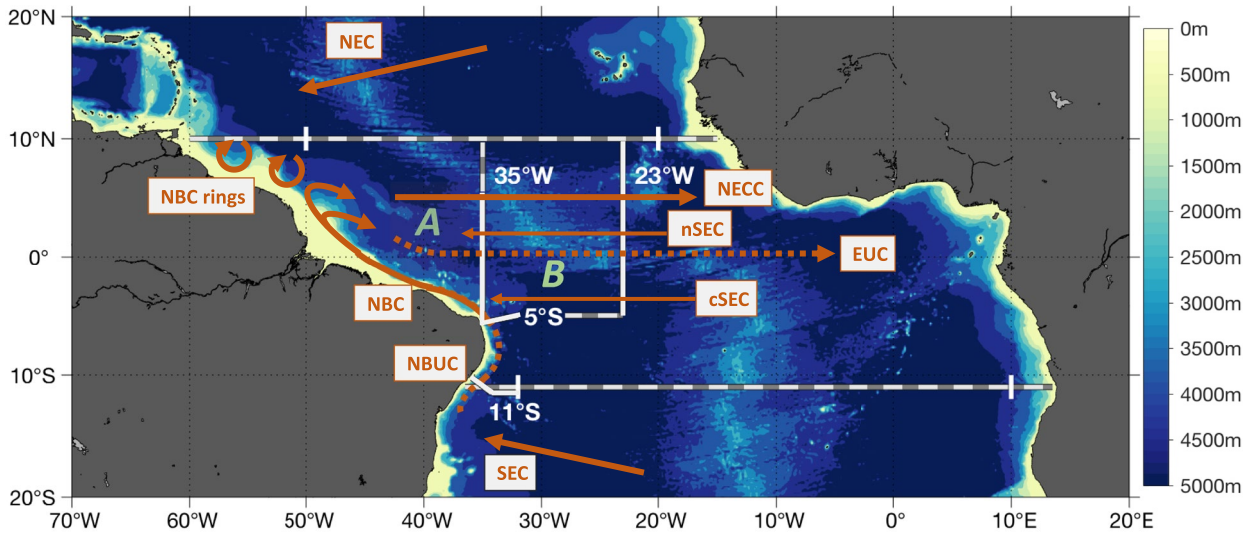

Figure 3. Bathymetry and schematic representation of the key surface (solid red arrows) and subsurface (dotted red arrows) currents and circulation components in the tropical upper Atlantic Ocean including the South Equatorial Current (SEC), North Brazil Undercurrent (NBUC), North Brazil Current (NBC), central South Equatorial Current (cSEC), Equatorial Undercurrent (EUC), northern South Equatorial Current (nSEC), North Equatorial Counter Current (NECC), North Brazil Current (NBC) rings and the North Equatorial Current (NEC). This schematic is based on the diagrams by Schott et al. (2002) and Dengler et al. (2004). Solid white lines indicate where current velocity measurements along repeated ship sections are available (11°S, 5°S, 35°W, and 23°W). Gray-and-white lines mark sections at which absolute geostrophic velocities are derived from hydrographic Argo float data. Both zonal sections are divided into a western boundary, an interior, and an eastern boundary subsection following Tuchen et al. (2020). Two boxes (denoted by A and B) are enclosed by different combinations of Argo and ship sections to estimate the transport budgets shown in Figure 11.

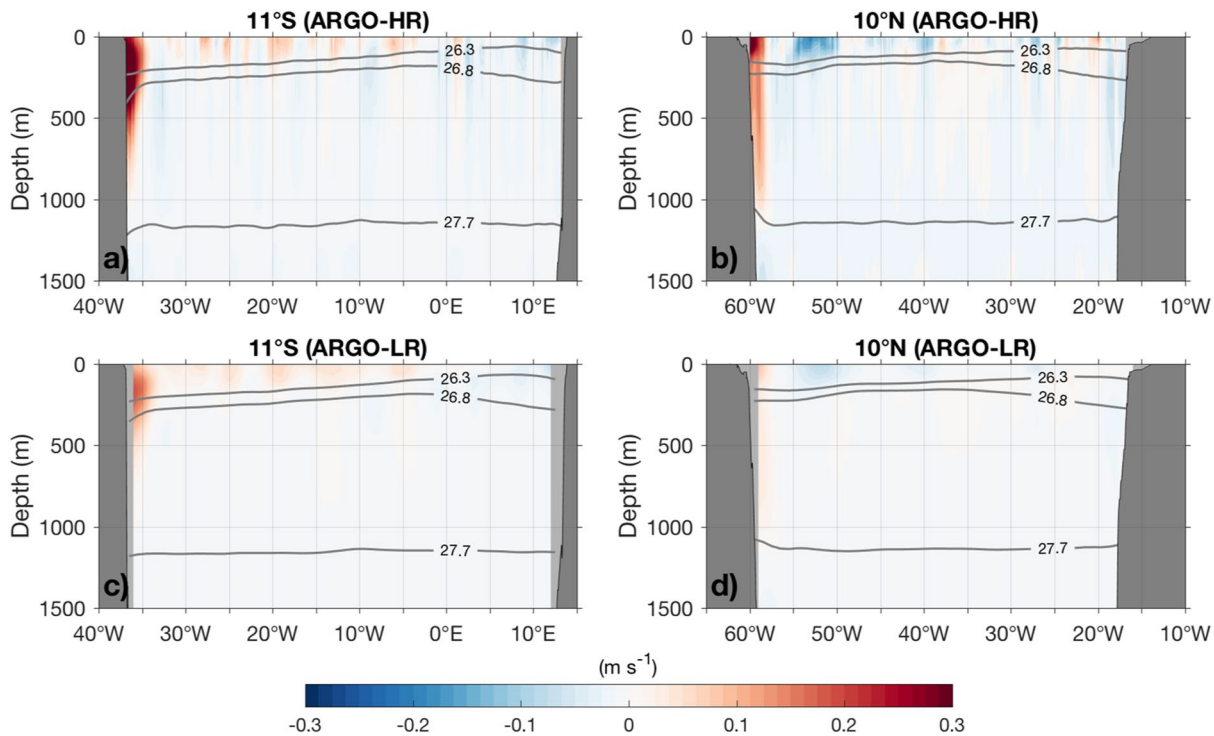

Figure 4. Absolute meridional geostrophic velocity sections derived from the Roemmich & Gilson Argo means along (a), (c) 11°S and (b), (d) 10°N for the (a), (b) 1/6° horizontal resolution product (ARGO-HR) and (c), (d) the 1° horizontal resolution product (ARGO-LR). Solid thick lines represent neutral density surfaces and separate water masses according to Table 1. A reference level of no motion at 1,200 m is applied (approximating the 27.7 $kg\,m^{-3}$ isopycnal).

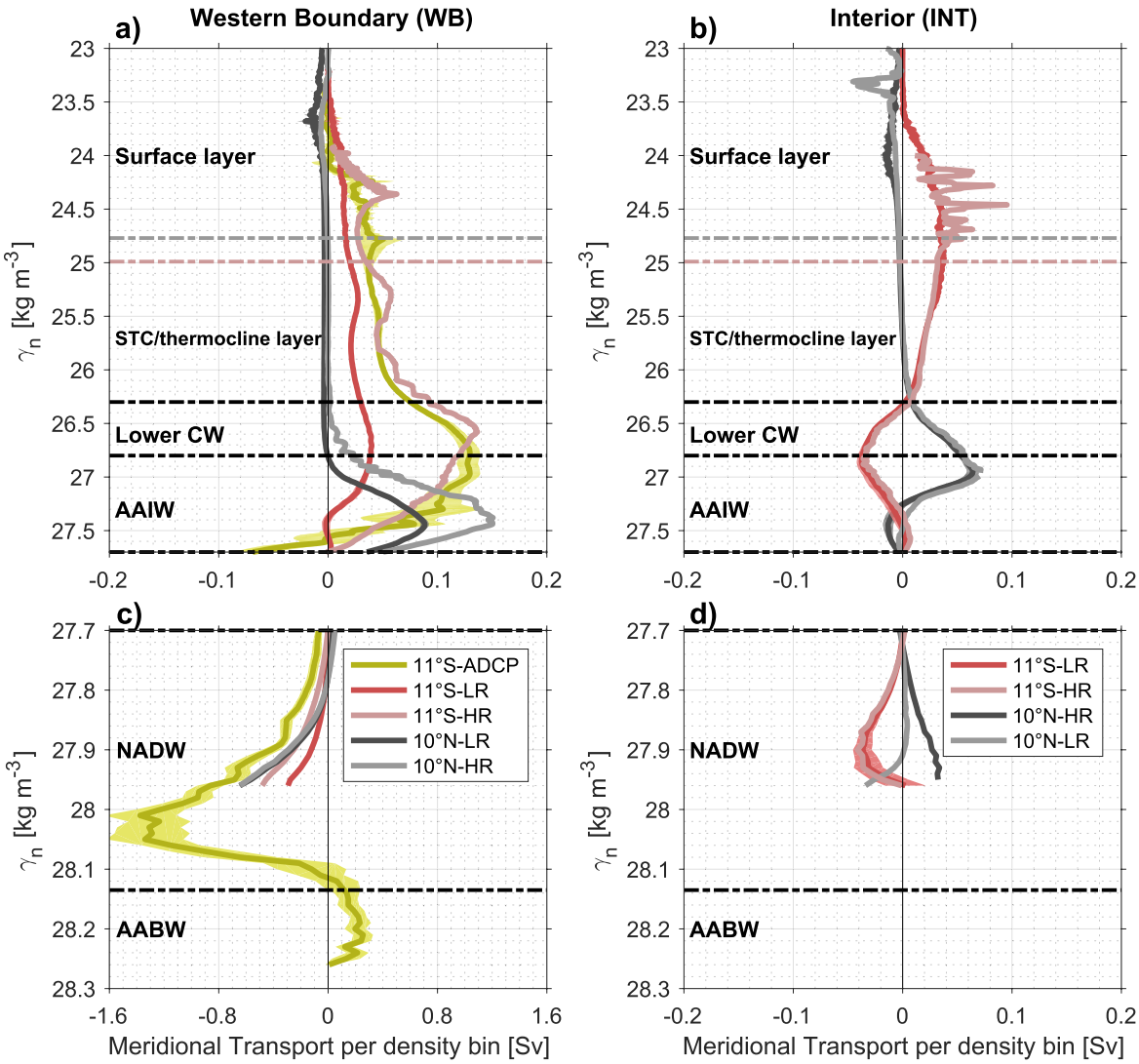

Figure 5. (a), (c) Western boundary (WB) and (b), (d) interior mean meridional volume transport within 0.01 $kg\,m^{-3}$ neutral density bins from Argo data at 11°S (reddish) and 10°N (greyish) derived at different resolutions and from western boundary shipboard velocity data at 11°S (yellow). The western boundary at 11°S (10°N) is defined as west of 32°W (50°W) while the interior at 11°S (10°N) is defined as eastward of 32°W (50°W) and westward of 9°E (20°W). Note that both axes change below a neutral density of 27.7 $kg\,m^{-3}$ (marking the interface between the upper and the lower branch of the AMOC). Individual water mass layers are generally separated by isopycnals (black dashed-dotted lines) except for the lower boundary of the surface layer which is originally defined as a depth (see Table 1) and, here, converted into neutral density space marked by the red (gray) dashed-dotted line for 11°S (10°N). The standard error of the mean envelope is given for the monthly varying ARGO-LR and ship-based transports for each density bin.

noted for the STC layer by Tuchen et al. (2019). In contrast, the vertical profile of meridional transport derived from ARGO-HR is generally in good agreement with the ship-based meridional transport profile and the overall vertical structure of meridional transport is well reproduced. However, the maximum northward transport which is associated with the core of the NBUC is slightly shallower in ARGO-HR where it is observed within the lower CW layer.

Although a comparable observational reference is not available for the western boundary in the tropical northern hemisphere, we still observe a substantial increase of northward transport at the western boundary at 10°N when using ARGO-HR instead of ARGO-LR indicating a general underestimation of western boundary transports in the lower-resolved Argo product. Nevertheless, both ARGO-HR and ARGO-LR agree on a similar vertical structure at the western boundary at 10°N with maximum northward transport observed within the AAIW layer. The absence of northward transport at thermocline level at the northern hemisphere tropical western boundary has already been noted in the observational analysis of Wilson and Johns (1997) and by the model experiments of

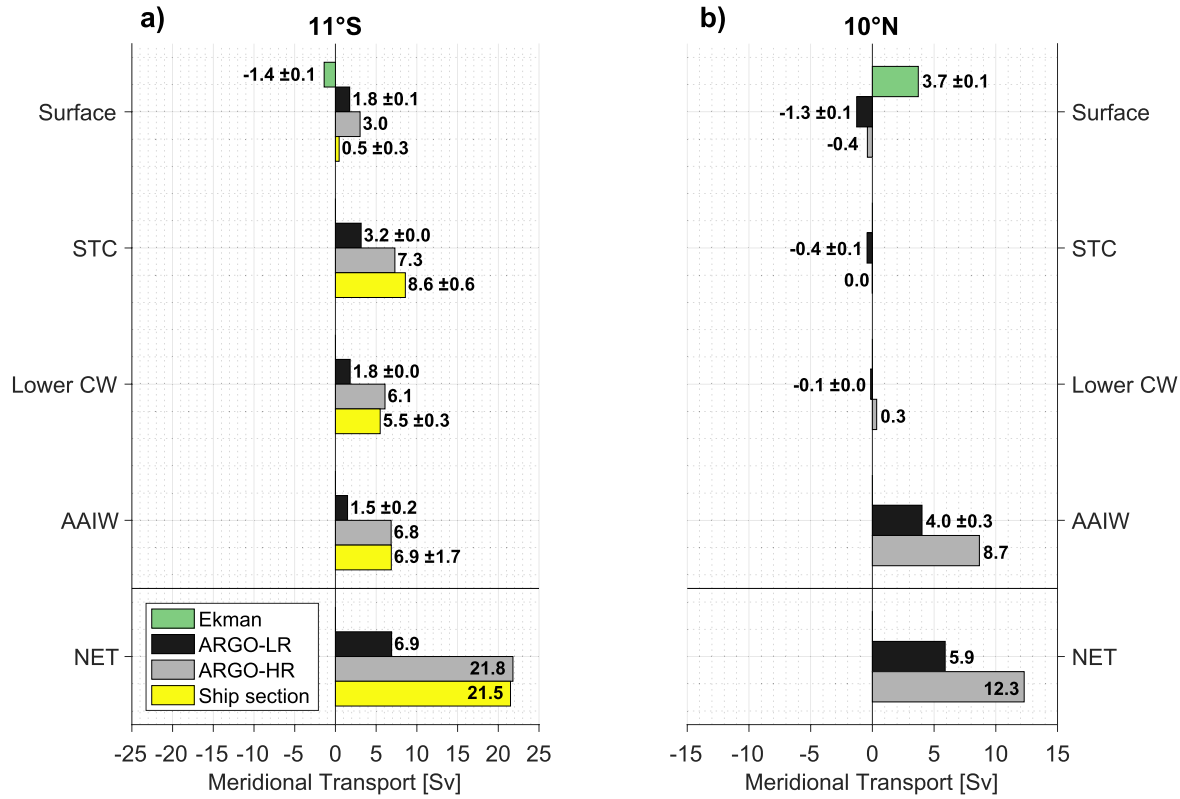

Figure 6. Meridional layer transports at the western boundary across (a) 11°S and (b) 10°N according to the definitions of Table 1. An Ekman transport contribution (green bars) is added to the surface layer as well as net transports for each data set including Ekman and geostrophic transports at the bottom. Positive (negative) values represent northward (southward) volume transport. The standard error of the mean is given for the monthly varying ARGO-LR, the weekly varying Ekman and the ship section transport estimates.

Jochum and Malanotte-Rizzoli (2001). Note here, that the surface layer transports derived from ARGO-HR and ARGO-LR in Figures 5a and 5b do not include an Ekman component. Total layer transports including geostrophic and Ekman transport components for the surface layer will be presented and discussed in more detail below.

Away from the western boundary, the analysis of meridional transports observed in the interior and eastern boundary part of the zonal sections at 11°S and 10°N only shows small differences between ARGO-HR and ARGO-LR transports in the upper 1,200 m at both latitudes (Figures 5b and 5d and S4 in Supporting Information S1). The importance of using higher horizontal resolution data to realistically resolve the vertical structure of the observed circulation applies exclusively to the western boundary. In order to compare total transports of the individual water mass layers, the vertical profiles of meridional transport are integrated within the vertical extent of the return flow layers as defined in Table 1 (Figure 6). In the surface layers, the meridional Ekman transport is also included, which opposes the surface layer meridional geostrophic transport at both latitudes (see also Figure 1). In all four layers (surface, STC/thermocline, lower CW, AAIW), meridional transports at the western boundary at 11°S derived from ARGO-HR and meridional transports derived from the mean ship section are in good agreement. This is not the case for meridional transports derived from ARGO-LR that largely underestimate the observed transports especially below the surface layer. In total, a northward transport of 21.8 (21.5 ± 2.2) Sv is observed by ARGO-HR + Ekman (mean ship section) entering the inner tropics (here defined as between 11°S and 10°N) at the western boundary at 11°S. Although previous studies provide observational evidence for the direct throughflow of southern hemisphere waters along the western boundary (Bourlès et al., 1999; Schott et al., 1998), a considerable fraction of these waters follow a more complex pathway of recirculation within the tropical zonal current system before eventually leaving the inner tropics which will be further discussed in Section 6.

At the western boundary at 10°N (westward of 50°W), most of the observed northward transport is accomplished through northward Ekman transport within the surface layer and by northward geostrophic transport within the

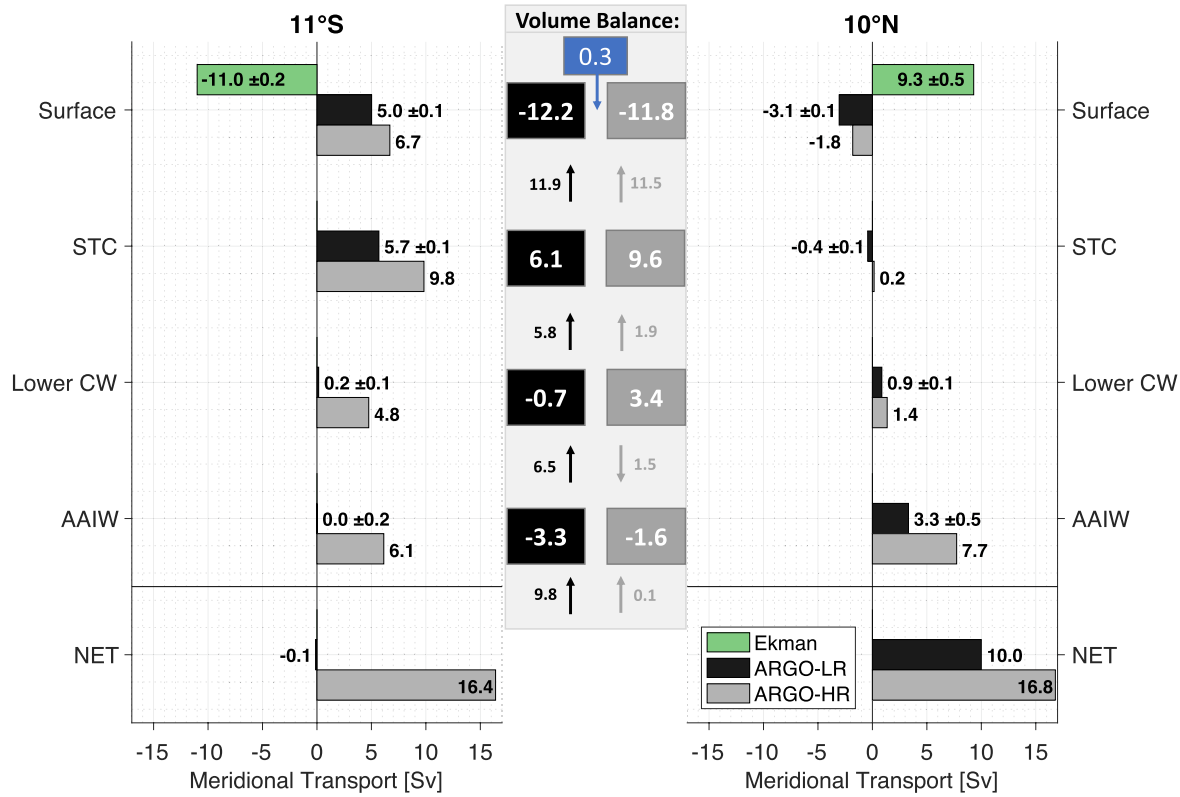

Figure 7. Meridional layer transports across the zonal sections at 11°S (left panel) and 10°N (right panel) and associated diapycnal transports (Sv) in between these latitudes (middle panel). The overall net transports for each data set, including Ekman and geostrophic transports, are given at the bottom of both panels. Positive (negative) values represent northward (southward) volume transport. The volume balances (squares; positive (negative) values indicate a convergence (divergence) of volume) and resulting diapycnal transport estimates (arrows) are given for the high-resolution (gray) and the low-resolution (black) Argo product based on the assumption of volume conservation within each individual water mass layer (see text for more detail). The surface layer volume budget also includes the freshwater supply due to precipitation, evaporation and river runoff (blue square) according to Dai and Trenberth (2003). The standard error of the mean is given for the monthly varying ARGO-LR and the weekly varying Ekman transport estimates.

AAIW layer (Figure 6b). Interestingly, the STC/thermocline layer and lower CW layer hardly show any meridional net transports. This is likely a consequence of the retroflection of the NBC that compensates northward transports close to the western boundary in these layers and/or that these water masses are supplied to the tropical zonal current system before even reaching the western boundary at 10°N. A total of 12.3 Sv (ARGO-HR + Ekman) is leaving the inner tropics at the western boundary at 10°N. Before further investigating the observed mean transports and pathways, we first focus on the diapycnal transports of the individual water masses within the AMOC return flow from entering to leaving the tropical and equatorial current system between 11°S and 10°N.

5. Diapycnal Transport Within the Tropical AMOC Return Flow

The AMOC return flow enters the inner tropics predominantly at the western boundary (see Figures 6a and 9a). In total, we find an AMOC return flow of 16.4 Sv (16.8 Sv) across 11°S (10°N) based on ARGO-HR geostrophic transports and satellite-derived Ekman transports (Figure 7). At 10°N, only about 60% of the observed northward transport of the AMOC return flow is leaving the inner tropics through the western boundary pathway. Clearly, the passage of a considerable fraction of the return flow through the tropical Atlantic is more complex and likely involves recirculation in the inner tropics which favors mixing and transformation of water mass properties by a prolonged residence time within the equatorial current system. Building up on the validation of ARGO-HR in the previous section, this data set is further explored in this section to investigate the tropical upwelling of the AMOC return flow between 11°S and 10°N.

Based on the zonal sections of meridional geostrophic velocity along 11°S and 10°N derived from both Argo products and complemented by Ekman transport in the surface layer, an analysis of diapycnal transports within

the inner tropics is carried out as follows: under the assumption that each vertical layer of the AMOC return flow (see Table 1) conserves its volume (taking into account precipitation, evaporation and river runoff to the upper layer volume budget), the vertical exchange rates, that is, diapycnal transports, between the water mass layers are derived. Figure 7 shows the meridional transport components (integrated from the western to the eastern boundary of the basin) across 11°S and 10°N and for ARGO-HR and ARGO-LR. In the surface layer, the meridional Ekman transport across these sections derived from the 2008–2020 ASCAT mean wind stress is included. At 11°S, the vertically integrated transport is found to be about zero for the ARGO-LR product which is in large disagreement with a northward AMOC return flow transport of 16.4 Sv observed in ARGO-HR. For each layer, the sum of all meridional transport components across the southern hemisphere section and across the northern hemisphere section yields either a transport divergence depicted by negative values or a transport convergence depicted by positive values.

For instance, in the surface layer and for ARGO-HR a net transport divergence of 11.8 Sv arises from the sum of 8.5 Sv geostrophic transport convergence and 20.3 Sv Ekman transport divergence, and is complemented by 0.3 Sv freshwater supply due to precipitation, evaporation and river runoff (Dai & Trenberth, 2003). This net divergence of transport must be compensated for by upwelling from the underlying layer, which is the STC/thermocline layer showing a transport convergence of 9.6 Sv largely driven by the pronounced equatorward transport across 11°S of the southern hemisphere Subtropical Cell. Interestingly, in a zonal average the northern hemisphere Subtropical Cell is close to being absent which is a consequence of the compensation of southward transport in the retroflection area by northward transport at the western boundary. In fact, equatorward transport associated with the northern hemisphere STC flow tends to cross 10°N in the vicinity of the retroflection (Tuchen et al., 2019). After supplying the required 11.5 Sv to the surface layer, the STC/thermocline layer exhibits a volume deficit of 1.9 Sv that must be upwelled from the lower CW layer. Notably, the ARGO-HR and ARGO-LR analyses show an increasing discrepancy of the estimated diapycnal transports with depth (Figure 7). Here, we are particularly interested in the diapycnal upwelling rate of lower CW into the STC/thermocline layer that has been previously estimated to be of the order of 6 Sv (Roemmich, 1983). In this study, we find a diapycnal transport of 1.9 Sv (ARGO-HR) which is about a third of the previously estimated transformation rate that is often mentioned in STC estimates to account for the diapycnal transport between the latitudes of estimation. A comparable diapycnal transport as observed by Roemmich (1983) is estimated when using ARGO-LR (5.8 Sv) suggesting that sparse horizontal resolution, which is especially crucial at the western boundary, could lead to such high transport estimates. However, the observed upwelling estimate from ARGO-LR is a direct consequence of unrealistic horizontal transports especially at 11°S.

6. Mean Transports and Pathways of the Tropical AMOC Return Flow

The previous sections emphasized the role of the western boundary for the AMOC return flow as the dominant pathway to enter the inner tropical Atlantic. However, the question arises where and how the AMOC return flow exits the inner tropics in terms of preferred vertical layers and longitudes. First, we extend the presented analysis of western boundary water mass layer transports to the interior and eastern boundary subsections along 11°S and 10°N (Figures 8 and 9). The interior part along 10°N is dominated by northward Ekman transport in the surface layer that is only slightly reduced by southward geostrophic transport (Figure 8b). At thermocline level, the northern hemisphere STC shows close to zero equatorward transport when not including longitudes within the NBC retroflection. In the lower CW and AAIW layer, both ARGO-HR and ARGO-LR show northward transports. When combined with the upper layer transports, a net northward transport of 8.5 Sv (ARGO-HR) is observed for the interior part of the 10°N section.

Across the interior part of the 11°S section, a strong southward Ekman transport of about 9.7 Sv is partially balanced by equatorward geostrophic transports in the surface and STC/thermocline layer (Figure 8a) in accordance with STC dynamics (Schott et al., 2004). As a consequence, a net southward transport of 3.4 Sv (ARGO-HR) is observed. The eastern boundary regions at 11°S and 10°N are generally dominated by southward geostrophic and Ekman transports of smaller magnitudes (Figure 9). Interestingly, the AAIW layer is the main component of the observed 4.0 Sv (ARGO-HR) of southward transport at the eastern boundary at 10°N. At the eastern boundary at 11°S, southward transports are small in all layers and add up to 2.0 Sv (ARGO-HR) further emphasizing the dominating role of the western boundary as a bottleneck for northward net transports associated with the AMOC return flow.

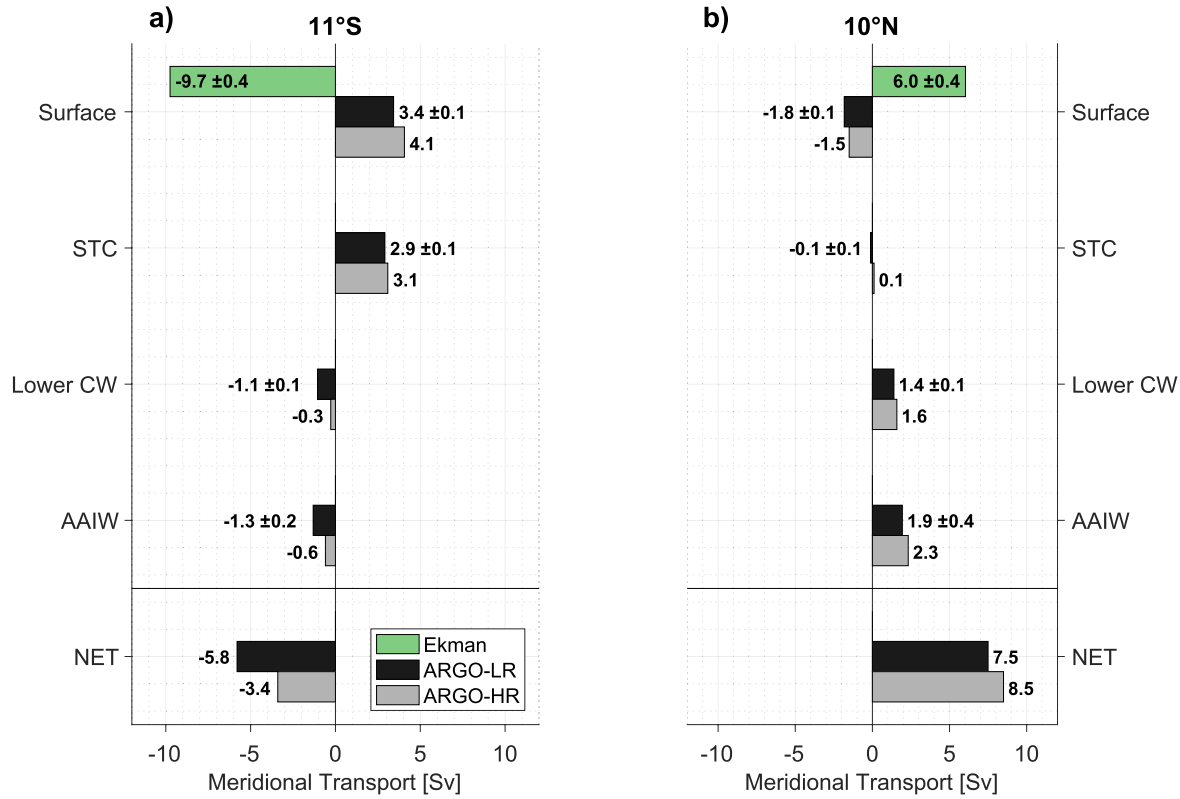

Figure 8. Meridional layer transports across the interior part of (a) 11°S and (b) 10°N according to the definitions of Table 1. An Ekman transport contribution (green bars) is added to the surface layer as well as net transports for each data set including Ekman and geostrophic transports at the bottom. Positive (negative) values represent northward (southward) volume transport. The standard error of the mean is given for the monthly varying ARGO-LR and the weekly varying Ekman transport estimates.

The pathways of the AMOC return flow after entering the inner tropics are further elucidated by additional current velocity data from repeated ship sections along 5°S (Figure 10a), 35°W (Figure 10b), and 23°W (Figure 10c) that all represent averages from at least 15 individual sections of shipboard velocity measurements from different years and seasons (see Figure 3 for a map of these sections). At 5°S, an intensified western boundary current is observed when compared to 11°S, characterized by a total northward transport of 25.3 ± 1.8 Sv across the zonal extent of the ship section and from the surface to 1,200 m. Similarly, the 35°W zonal velocity section, which is based on the shipboard velocity measurements described in Hormann and Brandt (2007) and Eden and Dengler (2008), shows a pronounced and deep-reaching western boundary current (Figure 10b). The 35°W section covers both the western boundary current system at the southernmost part of the meridional section where it reaches the continental shelf and the equatorial zonal current system away from the coastal areas.

Both cross-equatorial sections at 35°W and 23°W reveal main features of the equatorial current system, that is, a pronounced eastward Equatorial Undercurrent (EUC) in the thermocline to lower central water layer flanked by the central and northern branches of the SEC at the surface, and the intermediate current system between 400 and 1,000 m with alternating zonal currents. The alternating structure of the zonal currents are indicative of a large zonal exchange of mass across the equatorial Atlantic and within the AMOC return flow layer.

As further shown below, the eastward transport of thermocline and lower central water mainly manifests in the EUC, whereas intermediate water is dominantly transported westward within the EIC. Also, when dividing the 23°W section into two subsections north and south of 2°N (not shown) we observe westward transport north of 2°N while the southern subsection shows increased eastward transport, highlighting the role of the EUC in transporting and exchanging thermocline and lower central water from the western boundary towards the eastern part of the basin. On its eastward path the EUC shoals significantly (e.g., Johns et al., 2014) partly contributing to the zonally averaged upwelling within the upper layers of the AMOC return flow. These upwelled waters are then transported away from the equator mainly by poleward Ekman transport in the surface layer.

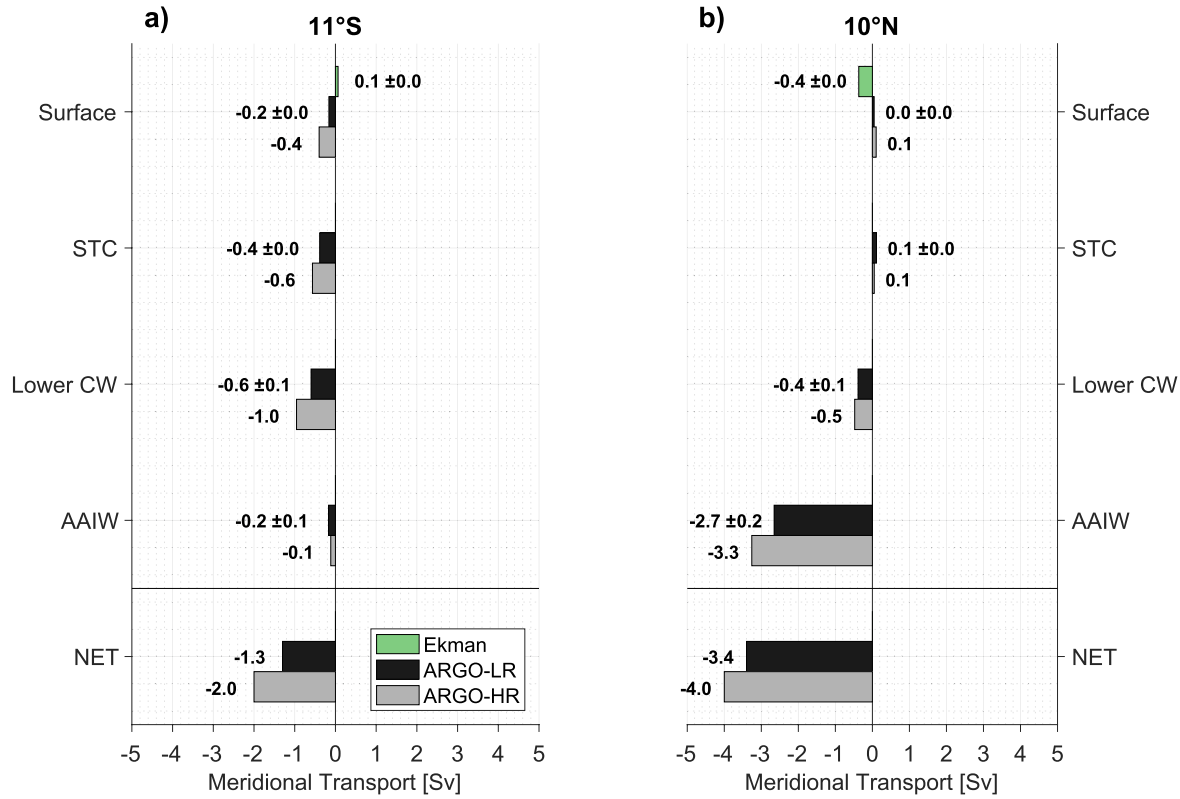

Figure 9. Meridional layer transports across the eastern part of (a) 11°S and (b) 10°N according to the definitions of Table 1. An Ekman transport contribution (green bars) is added to the surface layer as well as net transports for each data set including Ekman and geostrophic transports at the bottom. Positive (negative) values represent northward (southward) volume transport. The standard error of the mean is given for the monthly varying ARGO-LR and the weekly varying Ekman transport estimates.

To highlight the transport pathways of the individual water mass layers within the tropical AMOC return flow and to summarize their transport contributions, we examine the mass budgets within two particular domains (indicated by boxes A and B in Figure 3). Both boxes are bounded by a combination of ARGO-HR and repeated ship sections. If available, we use velocity data from repeated ship sections (in combination with surface drifter velocities as described in Section 3) and fill gaps in data coverage by geostrophic velocity data from ARGO-HR (in combination with wind-driven Ekman transports). For each box and layer, the incoming and outgoing transports across the individual surrounding sections are presented in Figure 11. Here, we combined the upper three layers (surface, STC/thermocline and lower CW) to focus on the differences between the upper-ocean (Figure 11a) and the intermediate layer (Figure 11b). At the western boundary, both layers are dominated by a northward transport across 11°S and further increased northward transport across 5°S where about 4–5 Sv are recirculated southward farther offshore in both layers, respectively. Through the southern part of the 35°W section waters continue to flow north- and westward. However, within the upper layers at 35°W away from the boundary, the flow is dominated by the eastward EUC which reduces the net westward transport across 35°W to 6.8 Sv. In fact, dividing the net transport through the 35°W section into its eastward and westward transport contributions (23.0 Sv eastward, 29.8 Sv westward) reveals a substantial zonal exchange of water masses within the upper layers. In these layers, a large part of the net north- and westward flowing water masses is retroflected back south- and eastward at the western boundary after crossing the equator to supply the North Equatorial Counter Current (NECC) and EUC as indicated by large eastward transports across the 23°W section of 28.9 Sv.

Overall, in combination with observed westward transports of 20.4 Sv, we find a net eastward transport of 8.5 Sv across the upper layers at 23°W. This is in contrast to the intermediate level at which we observe a net westward transport of 7.4 Sv across 23°W dominated by the Equatorial Intermediate Current (EIC) that is partly supplied by southward transport across the eastern boundary at 10°N and by recirculation of the flanking eastward intermediate currents. In total, we observe 30.1 Sv of westward transport and 22.7 Sv of eastward transport at intermediate level at 23°W indicating a substantial zonal exchange of mass.

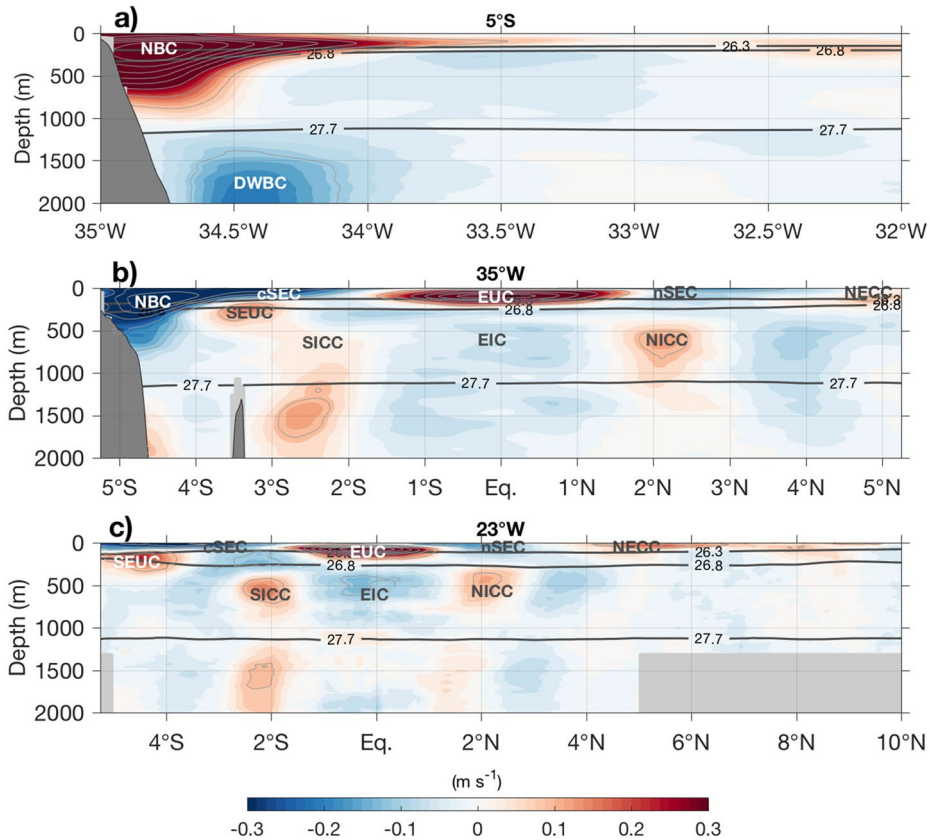

Figure 10. Mean ship section of (a) meridional velocity across 5°S, and zonal velocity across (b) 35°W and (c) 23°W. The mean ship section across 5°S is an average of 15 individual sections between 1990 and 2019 (see Table S6 in Supporting Information S1). The mean ship section across 35°W is an average of 16 individual sections between 1990 and 2006 as described by Hormann and Brandt (2007) and Eden and Dengler (2008) (see Table S7 in Supporting Information S1). The mean ship section across 23°W is an average of 27 individual sections between 2000 and 2018 (see Table S8 in Supporting Information S1). Solid thick lines represent neutral density surfaces and separate water masses according to Table 1. Dashed contours mark the zero-velocity line. The most important currents are marked in the figure: The North Brazil Current (NBC), South Equatorial Undercurrent (SEUC), central South Equatorial Current (cSEC), northern South Equatorial Current (nSEC), Equatorial Undercurrent (EUC), North Equatorial Counter Current (NECC), Southern Intermediate Counter Current (SICC), Equatorial Intermediate Current (EIC), Northern Intermediate Counter Current (NICC), and the Deep Western Boundary Current (DWBC).

Based on these transports, the most important pathways for the upper-ocean layer and the intermediate layer are highlighted schematically in Figure 11: in the upper-ocean, water enters the inner tropical Atlantic at the western boundary where it flows northward across 5°S and north-westward across 35°W. At 10°N, one part continues northward while another substantial part retroflects back southeastward and, in combination with the western boundary route of the northern hemisphere STC, supplies the eastward equatorial surface and subsurface currents along which these waters lose their density and upwell. Eventually, poleward Ekman transports remove these waters from the equatorial region at the surface. At intermediate level, AAIW enters the tropics at the western boundary at 11°S as well. Across 5°S, a partial recirculation of AAIW occurs, but the majority continues north-westward along the western boundary as observed at 35°W and also further north at 10°N. Away from the western boundary, the equatorial intermediate current system, and especially the EIC, transports and recirculates large amounts of intermediate water across the tropical Atlantic. A small portion of intermediate water is supplied through the eastern boundary at 10°N which could be partly of southern hemisphere origin indicating a cross-basin pathway of AAIW north of 10°N.

Finally, we summarize the presented transports for the combined upper-ocean and intermediate layers and provide an overview of the preferred AMOC return flow pathways based on ARGO-HR and shipboard velocity measurements (Figure 12). Here, geostrophic velocities from ARGO-HR are depth-averaged over the whole return flow

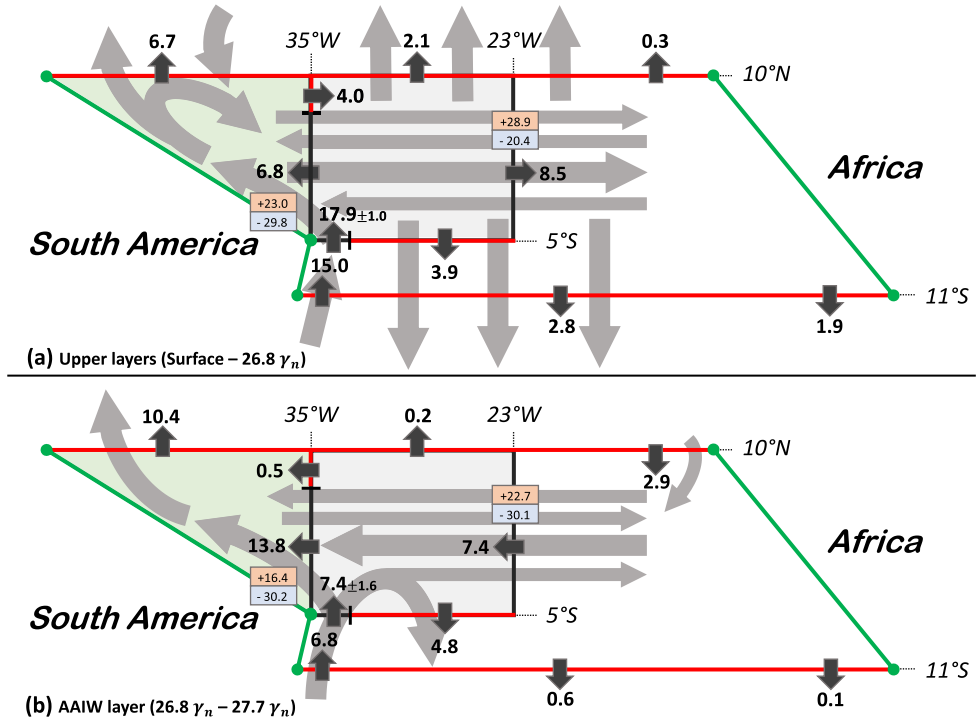

Figure 11. Schematic of boxes A (green shaded) and B (gray shaded) both introduced in Figure 3 and associated incoming and outgoing transports (in Sv) for (a) the upper-ocean layer consisting of the surface layer, Subtropical Cell/thermocline layer and lower CW layer and (b) the Antarctic Intermediate Water layer specified in Table 1 from ARGO-HR sections (red lines) and ship sections (black lines). Here, the South American and African coastlines are schematically represented by the green lines. ARGO-HR transports in (a) also include the Ekman transport component. Transports across 5°S include an uncertainty range being the standard error of the mean. To highlight the zonal exchange across the meridional ship sections of 35°W and 23°W the net transports are divided into eastward (red box) and westward (blue box) transport contributions. The inferred pathways of both layers are schematically indicated by the shaded gray arrows.

layer (surface to 27.7 $kg\,m^{-3}$) to illustrate the net geostrophic flow at each grid point. The most prominent circulation feature is the continuous northward western boundary current fed by the bifurcation of the South Equatorial Current between 15°S and 20°S. After crossing the equator, the return flow weakens and partially retroflects southeastward to supply the eastward surface and subsurface currents shown in Figures 10b and 10c. The western boundary current continues across the 10°N section and part of it enters the Caribbean seas. The overview in Figure 12 also includes the net meridional transport (Ekman + geostrophy) at each subsection (Western boundary [WB], interior [INT], eastern boundary [EB]) of the 11°S and 10°N ARGO-HR sections as well as total transports across the ship section at 5°S (meridional) and at 35°W and 23°W (both zonal). Additionally, the transports of ARGO-HR (+Ekman) along 10°N, 5°S and 35°W used for the analysis in Figure 11 are also shown. The role of the wind-driven transport component is especially pronounced along the interior subsection at 10°N where Ekman flow is the main component of the observed net northward transport, as well as along the interior subsection at 11°S where Ekman transport overcompensates the equatorward transport associated with the southern hemisphere STC.

7. Discussion

The presented results provide a first estimate of the mean transports, pathways and diapycnal transports of the AMOC return flow derived from a combination of Argo float data and shipboard velocity measurements. Here, we explore an updated version of the Argo data used in Zilberman et al. (2018) and show that it allows to realistically reconstruct the Atlantic Ocean western boundary circulation at 11°S as observed by shipboard velocity measurement along repeated sections (see Section 4).

The basin-wide intertropical exchange of mass associated with the northward flow of the upper branch of the AMOC has previously been described for the tropical Atlantic in studies based either on a limited number of

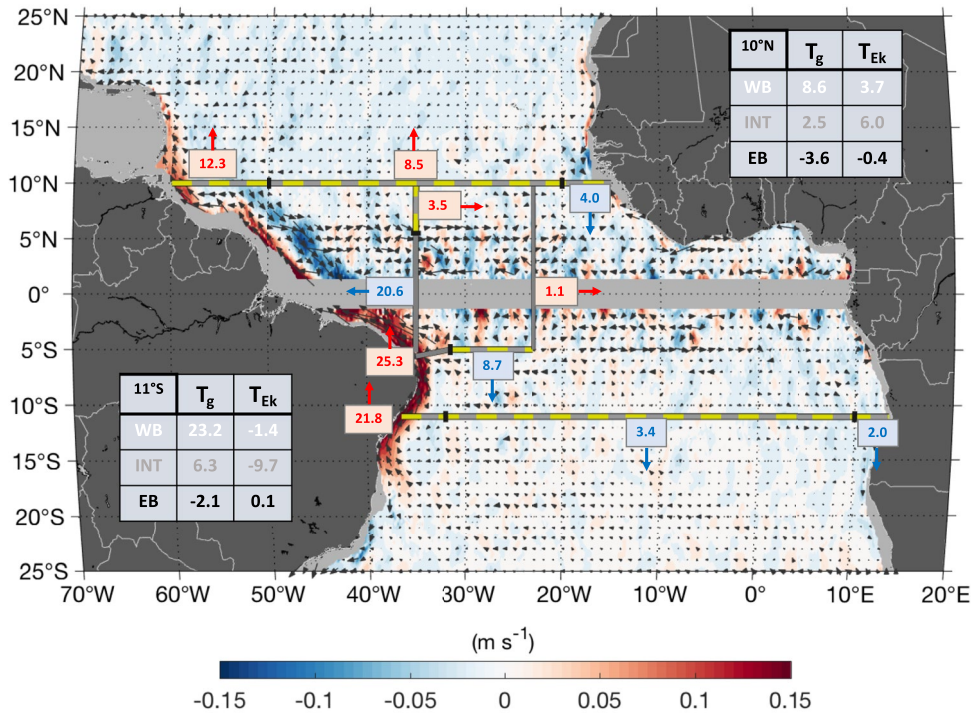

Figure 12. Mean geostrophic flow field within the Atlantic Meridional Overturning Circulation return flow layer (surface to 27.7 $kg\,m^{-3}$ isopycnal). Meridional velocities are represented by the shading and the horizontal flow is indicated by the arrows. Given in the squares are total meridional transports across 11°S and 10°N (yellow-gray lines) at the western boundary, in the interior ocean and at the eastern boundary in Sv as well as across selected zonal and meridional ship sections (gray lines). Red (blue) values indicate northward/eastward (southward/westward) transport. Total transports across ARGO-HR sections are the sum of geostrophic transport (T_g) and Ekman transport (T_{Ek}) as indicated in the tables.

in-situ measurements (Lux et al., 2001; Roemmich, 1983) or on ocean circulation models (e.g., Fratantoni et al., 2000; Malanotte-Rizzoli et al., 2000). From high-resolution (1/6°) Argo data and ASCAT wind stress, we derive a net northward transport of 16.4 Sv across 11°S, and 16.8 Sv across 10°N when considering both Ekman and geostrophic transport components over the full vertical extent of the AMOC return flow layer (see Table 1 and Figure 12) which is in very good agreement with, for instance, the results of Lumpkin and Speer (2007) who estimated a northward transport of 16.2 ± 3.0 Sv across 11°S. In contrast, Roemmich (1983) observed a net northward transport of about 10 Sv across four zonal sections at 8°N/S and 24°N/S. However, the transport estimates by Roemmich (1983) are based on individual ship sections carried out in the 1950s whereas the presented results of this study describe a mean estimate based on Argo observations between 2004 and 2018. Therefore, it is likely that the results of Roemmich (1983) are seasonally biased since AMOC transports show a substantial seasonal variability at tropical latitudes (e.g., Herrford et al., 2021). The results of Lux et al. (2001) are based on an inverse model from hydrographic measurements along two zonal sections at 7.5°N and 4.5°S. They find a northward transport of South Atlantic Water mainly through the NBUC of about 33 Sv. While such high transports are possible, the observed average northward transport of the NBUC based on ship section data is estimated to be about 26 Sv (Hummels et al., 2015). When extending the region farther offshore to include the offshore recirculation of the NBUC by using the full zonal extent of the ship section data used in Hummels et al. (2015), the mean transport is reduced to 21.5 ± 2.2 Sv.

From basin-wide zonal ship section data, the diapycnal transports between the individual layers can be estimated (see Section 5). Between 11°S and 10°N about 11.8 Sv of thermocline waters are upwelled into the surface layer (Figure 8) which is larger than the value of 7.5 Sv estimated by Lux et al. (2001) for the upwelling between 7.5°N and 4.5°S. The upwelling is directly linked to the observed Ekman divergence which varies between different wind products and for estimates at different latitudes. We find that 1.9 Sv of lower central water is upwelled into

the STC/thermocline layer which constitutes part of the tropical upwelling of the AMOC return flow and has to be considered in estimates of the STC circulation. Previously, the tropical upwelling of the AMOC return flow was estimated to be about three times larger (Roemmich, 1983) than the upwelling presented in this study.

In general, South Atlantic Water enters the upper inner tropical Atlantic via the western boundary current, that is, the NBUC/NBC at all layers above 1,200 m. In agreement with results from ship section data, we derive from ARGO-HR data a northward western boundary transport of 21.8 Sv mainly in the thermocline, lower central water and intermediate layer. Further north, the NBUC is supplied by westward surface currents and the current core shoals to form the surface-intensified NBC at around 5°S. From shipboard velocity data at 5°S, a mean northward transport of 25.3 ± 1.8 Sv is estimated which is somewhat underestimated by Argo data (not shown). Farther downstream, Schott et al. (2003) estimated a westward transport of 23.2 Sv in the upper 1,200 m across 35°W. The differences between the results of Schott et al. (2003) and a westward transport of 20.6 Sv, presented in this study, can be attributed to a new evaluation of the 35°W section data (Eden & Dengler, 2008) including additional sections and by the implementation of surface drifter velocities.

After crossing the equator, the NBC becomes unstable beyond ∼7°N and sheds northwestward propagating NBC rings (Garzoli et al., 2003, 2004; Johns et al., 2003). However, there is also evidence for a steady western boundary current in addition to the NBC rings (Garzoli et al., 2003). As a consequence, the net mass exchange across 10°N is believed to be accomplished by both a steady western boundary current and northwestward migrating NBC rings. Johns et al. (2003) found a generation of six rings per year with an annual mean eddy transport of about 9 Sv. By using the Argo mean, a separation between northward transport due to a steady western boundary current and northward transport due to the rectification of northwestward propagating NBC rings is not possible. In agreement with Zhang et al. (2003) we find a surface layer transport of 3–4 Sv across the western boundary at 10°N that is mainly driven by northward Ekman transport. At thermocline level, Zhang et al. (2003) observed a southward western boundary transport of about 3 Sv across 10°N. Here, we find a net transport of close to zero both for the thermocline and the lower central water layer. This discrepancy might be due to the data coverage close to the western boundary, where insufficient sampling could lead to an absence or underrepresentation of the northward steady western boundary current and, hence, could be biased toward southward transport due to the retroflection farther offshore. However, this disparity deserves further attention in another study.

The western boundary pathway marks the so-called direct route of the AMOC return flow for crossing the inner tropics. A more indirect route is described by a rather complex recirculation of South Atlantic Water within the equatorial zonal current system. When becoming unstable, the NBC is retroflected southeastward and dominantly supplies surface and thermocline/central water to the NECC and EUC, respectively (e.g., Hazeleger et al., 2003). In fact, we observe close to zero northward transport in these layers across the western boundary at 10°N in accordance with model results (Jochum & Malanotte-Rizzoli, 2001). The observational study of Wilson and Johns (1997) showed that a maximum of 6–8 Sv of South Atlantic water enters the Caribbean Sea through the southern passages predominantly in the surface layer, while the presented results show a northward transport of about 3 Sv in the surface layer, but a large inflow of intermediate water. One explanation for this disparity could be the role of the indirect route of the AMOC return flow that carries mainly surface water northward across 10°N where these waters join the westward North Equatorial Current (NEC) and reach the southern passage to enter the Caribbean Sea as also speculated by Wilson and Johns (1997). However, a main finding of their study and this work is that more observations and research are needed on the northern hemisphere pathways between the retroflection area and the Caribbean Sea. In total, a northward transport of 12.3 Sv is leaving the inner tropics through the western boundary at 10°N which represents about 60% of the observed northward transport at 11°S. Another 8.5 Sv is observed crossing 10°N in the interior.

8. Conclusions

In this study, the capability of hydrographic data from Argo floats to realistically reproduce the mean characteristics of the western boundary current in the tropical Atlantic Ocean has been demonstrated in a case study for the western boundary circulation at 11°S and then further applied to the tropical Atlantic to analyze the diapycnal transports of the AMOC return flow when crossing the tropics and its associated mean pathways and transports. We conclude the following key points:

1. High-resolution Argo data is necessary (a) to reconstruct the vertical structure of the western boundary circulation at 11°S and (b) to derive comparable transport estimates of the particular water mass layers within the AMOC return flow as observed by repeated ship section data. A horizontal resolution of 1/6° shows substantial improvements in representing the meridional transport at all vertical layers in comparison to the same Argo mean with a coarser horizontal resolution of 1°.
2. The observed tropical upwelling of the thermohaline circulation within the AMOC return flow layer from the lower CW layer into the STC/thermocline layer is estimated to be 1.9 Sv which is about a third of the previous estimate by Roemmich (1983). This diapycnal transport estimate has implications for STC estimates that are usually calculated at 10°N/S and rely on an estimate of the amount of water entering this layer in between these latitudes from below. The difference to earlier estimates is attributed to the improved horizontal resolution.
3. For the first time, an observational view of the mean pathways of the AMOC return flow in the inner tropical Atlantic is inferred from a combination of Argo float observations, shipboard velocity measurements and satellite wind data. At 11°S, 21.8 Sv enter the inner tropics through the western boundary of which a considerable fraction (12.3 Sv) also leaves the tropics through western boundary pathways at 10°N which is often called the direct route of the return flow. The indirect route describes the recirculation and transformation of southern hemisphere water within the western boundary current system and the equatorial Atlantic zonal current system, for example, the NECC and the EUC. Mainly through upwelling and northward Ekman transport, about 8.5 Sv exit the inner tropics through the interior pathway along 10°N.

The presented results provide a mean description of the tropical AMOC return flow. However, a time series of the geostrophic AMOC transport components from high-resolution Argo data to derive trends and long-term variability remains a challenge. The indirect route of the AMOC return flow bears a potential for providing a transport time series because only the western boundary circulation depends on high-resolution Argo float data while interior geostrophic transport estimates from lower-resolved Argo data, which are available on a monthly basis, are in good agreement with results from high-resolution Argo data.

The inferred transport values provide a valuable reference of tropical AMOC estimates against which model simulations could be validated and compared. The observed upwelling of the thermohaline circulation is not negligible in STC estimates, but also not as large as previously estimated from single zonal ship sections. A better description of the preferred pathways of the AMOC return flow in terms of zonal range and vertical layers is important for understanding the propagation of advective AMOC signals across the tropics and the equator which could be different for the particular water mass layers. It is further pointed out that the Argo program provides a fundamental data base for such studies and that the continuation of Argo float observations is needed to provide a spatially coherent representation of the observed upper-ocean circulation. Similarly, the ongoing observational efforts in collecting ship section data particularly across western boundary currents and the equator provide a valuable reference and need to be maintained.

Data Availability Statement

Hydrographic data from the Roemmich-Gilson Argo climatology are available and regularly updated under http://sio-argo.ucsd.edu/RG_Climatology.html. Here, we used the latest version of the climatological means for the period 2004–2018 (updated 17 January 2020). These data were collected and made freely available by the International Argo Program and the national programs that contribute to it (http://www.argo.ucsd.edu, http://argo.jcommops.org). The Argo Program is part of the Global Ocean Observing System. C-2015 ASCAT data are produced by Remote Sensing Systems and sponsored by the NASA Ocean Vector Winds Science Team. Data are available at www.remss.com. Near-surface current data from surface drifting buoys are available at https://www.aoml.noaa.gov/phod/gdp/mean_velocity.php. Here, we used version 3.06 released on 16th of November 2020 and accessed on 9th of August 2021. Ocean reanalysis data from ECMW-ORA-S4 can be accessed via ftp://ftp-icdc.cen.uni-hamburg.de/EASYInit/ORA-S4/monthly_1x1/. The presented mean zonal velocity section along 35°W is based on the individual sections described in Hormann and Brandt (2007) and shown in Eden and Dengler (2008). Most current velocity measurements at 11°S, 5°S, 35°W, and 23°W used in this study are available through the world data center PANGAEA collected under: https://doi.pangaea.de/10.1594/PANGAEA.937809. A complete list of research cruises and data sources is provided in the Tables S5, S6, S7, and S8 in Supporting Information S1. In order to better facilitate the reproducibility of the results, we are also providing the mean

current velocity sections along 11°S, 5°S, 35°W, and 23°W derived from shipboard measurements via zenodo (Tuchen et al., 2022): https://doi.org/10.5281/zenodo.5772272. Further information is given in the Supporting Information S1.

Acknowledgments
This study was supported by the German Federal Ministry of Education and Research (BMBF) as part of the BANINO project (03F0795A) and by the TRIATLAS project which has received funding from the European Union's Horizon H2020 research and innovation program under grant agreement 817578. The authors thank the captains, crews, scientists and technicians who contributed to collecting the observational data used in this study during numerous research cruises to the tropical Atlantic. The authors would also like to thank Kristin Burmeister for analyzing and providing shipboard velocity measurements at 23°W. The authors are grateful to two anonymous reviewers for their helpful comments and suggestions, which led to significant improvements of the manuscript.

References

Argo (2000). Argo float data and metadata from Global Data Assembly Centre (Argo GDAC). SEANOE. https://doi.org/10.17882/42182

Boers, N. (2021). Observation-based early-warning signals for a collapse of the Atlantic meridional overturning circulation. *Nature Climate Change*, *11*(8), 680–688. https://doi.org/10.1038/s41558-021-01097-4

Bourlès, B., Gouriou, Y., & Chuchla, R. (1999). On the circulation in the upper layer of the western equatorial Atlantic. *Journal of Geophysical Research*, *104*(9), 21151–21170. https://doi.org/10.1029/1999JC900058

Bower, A., Lozier, S., Biastoch, A., Drouin, K., Foukal, N., Furey, H., et al. (2019). Lagrangian views of the pathways of the Atlantic meridional overturning circulation. *Journal of Geophysical Research: Oceans*, *124*, 5313–5335. https://doi.org/10.1029/2019JC015014

Brandt, P., Hahn, J., Schmidtko, S., Tuchen, F. P., Kopte, R., Kiko, R., et al. (2021). Atlantic Equatorial Undercurrent intensification counteracts warming-induced deoxygenation. *Nature Geoscience*, *14*, 278–282. https://doi.org/10.1038/s41561-021-00716-1

Caesar, L., McCarthy, G. D., Thornalley, D. J. R., Cahill, N., & Rahmstorf, S. (2021). Current Atlantic meridional overturning circulation weakest in last millennium. *Nature Geoscience*, *14*, 118–120. https://doi.org/10.1038/s41561-021-00699-z

Chang, P., Zhang, R., Hazeleger, W., Wen, C., Wan, X., Ji, L., et al. (2008). Oceanic link between abrupt changes in The north Atlantic Ocean and the African monsoon. *Nature Geoscience*, *1*, 444–448. https://doi.org/10.1038/ngeo218

Cunningham, S. A., Kanzow, T., Rayner, D., Baringer, M. O., Johns, W. E., Marotzke, J., et al. (2007). Temporal variability of the Atlantic meridional overturning circulation at 26.5°N. *Science*, *317*, 935–938. https://doi.org/10.1126/science.1141304

da Silveira, I. C. A., Miranda, L. B., & Brown, W. S. (1994). On the origins of the north Brazil current. *Journal of Geophysical Research*, *99*, 22501–22512. https://doi.org/10.1029/94JC01776

Dai, A., & Trenberth, K. E. (2003). New estimates of continental discharge and oceanic freshwater transport. *17th Conference on Hydrology* (Vol. 11). American Meteorological Society. Retrieved from https://ams.confex.com/ams/annual2003/techprogram/paper_55037.htm

Dengler, M., Schott, F. A., Eden, C., Brandt, P., Fischer, J., & Zantopp, R. J. (2004). Break-up of the Atlantic deep western boundary current into eddies at 8°S. *Nature*, *432*, 1018–1020. https://doi.org/10.1038/nature03134

Dong, S., Baringer, M., Goni, G., & Garzoli, S. (2011). Importance of the assimilation of Argo float measurements on the meridional overturning circulation in the South Atlantic. *Geophysical Research Letters*, *38*, L18603. https://doi.org/10.1029/2011GL048982

Eden, C., & Dengler, M. (2008). Stacked jets in the deep equatorial Atlantic Ocean. *Journal of Geophysical Research*, *113*, C04003. https://doi.org/10.1029/2007JC004298

Frajka-Williams, E., Ansorge, I. J., Baehr, J., Bryden, H. L., Chidichimo, M. P., Cunningham, S. A., et al. (2019). Atlantic meridional overturning circulation: Observed transport and variability. *Frontiers in Marine Science*, *6*, 260. https://doi.org/10.3389/fmars.2019.00260

Fratantoni, D. M., Johns, W. E., Townsend, T. L., & Hurlburt, H. E. (2000). Low-latitude circulation and mass transport pathways in a model of the tropical Atlantic Ocean. *Journal of Physical Oceanography*, *30*(8), 19442–1966. https://doi.org/10.1175/1520-0485(2000)030<1944:llcamt>2.0.co;2

Fu, Y., Li, F., Karstensen, J., & Wang, C. (2020). A stable Atlantic meridional overturning circulation in a changing North Atlantic ocean since the 1990s. *Science Advances*, *6*(48), eabc7836. https://doi.org/10.1126/sciadv.abc7836

Garzoli, S. L., Ffield, A., Johns, W. E., & Yao, Q. (2004). North Brazil current retroflection and transports. *Journal of Geophysical Research*, *109*, C01013. https://doi.org/10.1029/2003jc001775

Garzoli, S. L., Ffield, A., & Yao, Q. (2003). North Brazil Current rings and the variability in the latitude of retroflection. *Interhemispheric Water Exchange in the Atlantic Ocean* (Vol. 68, pp. 357–373). Elsevier Oceanography Series. https://doi.org/10.1016/S0422-9894(03)80154-X

Hazeleger, W., de Vries, P., & Friocourt, Y. (2003). Sources of the Equatorial Undercurrent in a high-resolution ocean model. *Journal of Physical Oceanography*, *33*(4), 677–693. https://doi.org/10.1175/1520-0485(2003)33<677:soteui>2.0.co;2

Hazeleger, W., & Drijfhout, S. (2006). Subtropical cells and meridional overturning circulation pathways in the tropical Atlantic. *Journal of Geophysical Research*, *111*, C03013. https://doi.org/10.1029/2005JC002942

Herrford, J., Brandt, P., Kanzow, T., Hummels, R., Araujo, M., & Durgadoo, J. V. (2021). Seasonal variability of the Atlantic Meridional Overturning Circulation at 11°S inferred from bottom pressure measurements. *Ocean Science*, *17*, 265–284. https://doi.org/10.5194/os-17-265-2021

Hoegh-Guldberg, O., Jacob, D., Taylor, M., Bindi, M., Brown, S., Camilloni, I., et al. (2018). Impacts of 1.5ºC global warming on natural and human systems. In V. Masson-Delmotte, P. Zhai, H.-O. Pörtner, D. Roberts, J. Skea, P. R. Shukla (Eds.), *Global Warming of 1.5°C. An IPCC Special Report on the impacts of global warming of 1.5°C above pre-industrial levels and related global greenhouse gas emission pathways, in the context of strengthening the global response to the threat of climate change, sustainable development, and efforts to eradicate poverty*. Retrieved from https://www.ipcc.ch/sr15/chapter/chapter-3/

Hormann, V., & Brandt, P. (2007). Atlantic equatorial undercurrent and associated cold tongue variability. *Journal of Geophysical Research*, *112*, C06017. https://doi.org/10.1029/2006JC003931

Hummels, R., Brandt, P., Dengler, M., Fischer, J., Araujo, M., Veleda, D., & Durgadoo, J. V. (2015). Interannual to decadal changes in the western boundary circulation in the Atlantic at 11°S. *Geophysical Research Letters*, *42*, 7615–7622. https://doi.org/10.1002/2015GL065254

Jochum, M., & Malanotte-Rizzoli, P. (2001). Influence of the meridional overturning circulation on tropical-subtropical pathways. *Journal of Physical Oceanography*, *31*(5), 13132–1323. https://doi.org/10.1175/1520-0485(2001)031<1313:iotmoc>2.0.co;2

Johns, W. E., Baringer, M. O., Beal, L. M., Cunningham, S. A., Kanzow, T., Bryden, H. L., et al. (2011). Continuous, array-based estimates of Atlantic Ocean heat transport at 26.5°N. *Journal of Climate*, *24*(10), 2429–2449. https://doi.org/10.1175/2010JCLI3997.1

Johns, W. E., Brandt, P., Bourlès, B., Tantet, A., Papapostolou, A., & Houk, A. (2014). Zonal structure and seasonal variability of the Atlantic equatorial undercurrent. *Climate Dynamics*, *43*(11), 3047–3069. https://doi.org/10.1007/s00382-014-2136-2

Johns, W. E., Lee, T. N., Beardsley, R. C., Candela, J., Limeburner, R., & Castrom, B. (1998). Annual cycle and variability of the North Brazil current. *Journal of Physical Oceanography*, *28*(1), 1032–128. https://doi.org/10.1175/1520-0485(1998)028<0103:acavot>2.0.co;2

Johns, W. E., Zantopp, R. J., & Goni, G. J. (2003). Cross-gyre transport by North Brazil current rings. *Interhemispheric Water Exchange in the Atlantic Ocean* (Vol. 68, pp. 411–441). Elsevier Oceanography Series. https://doi.org/10.1016/S0422-9894(03)80156-3

Laurindo, L., Mariano, A., & Lumpkin, R. (2017). An improved near-surface velocity climatology for the global ocean from drifter observations. *Deep-Sea Research Part I*, *124*, 73–92. https://doi.org/10.1016/j.dsr.2017.04.009

Lenton, T. M., Held, H., Kriegler, E., Hall, J. W., Lucht, W., Rahmstorf, S., & Schellnhuber, H. J. (2008). Tipping elements in the Earth's climate system. *Proceedings of the National Academy of Sciences*, *106*(49), 20561–1793. https://doi.org/10.1073/pnas.0705414105

Lozier, M. S., Li, F., Bacon, S., Bahr, F., Bower, A. S., Cunningham, S. A., et al. (2019). A sea change in our view of overturning in the subpolar North Atlantic. *Science*, *363*, 516–521. https://doi.org/10.1126/science.aau6592

Lumpkin, R., & Speer, K. (2007). Global ocean meridional overturning. *Journal of Physical Oceanography*, *37*(9), 2550–2562. https://doi.org/10.1175/JPO3130.1

Lux, M., Mercier, H., & Arhan, M. (2001). Interhemispheric exchanges of mass and heat in the Atlantic Ocean in January–March 1993. *Deep-Sea Research Part I: Oceanographic Research Papers*, *48*(3), 605–638. https://doi.org/10.1016/S0967-0637(00)00033-9

Luyten, J., Pedlosky, J., & Stommel, H. (1983). The ventilated thermocline. *Journal of Physical Oceanography*, *13*(2), 292–309. https://doi.org/10.1175/1520-0485(1983)013<0292:tvt>2.0.co;2

Malanotte-Rizzoli, P., Hedstrom, K., Arango, H., & Haidvogel, D. B. (2000). Water mass pathways between the subtropical and tropical ocean in a climatological simulation of the North Atlantic Ocean circulation. *Dynamics of Atmospheres and Oceans*, *32*(3–4), 331–371. https://doi.org/10.1016/S0377-0265(00)00051-8

Meinen, C. S., Speich, S., Piola, A. R., Ansorge, I., Campos, E., Kersalé, M., et al. (2018). Meridional overturning circulation transport variability at 34.5°S during 2009–2017: Baroclinic and barotropic flows and the dueling influence of the boundaries. *Geophysical Research Letters*, *45*, 4180–4188. https://doi.org/10.1029/2018GL077408

Moat, B. I., Smeed, D. A., Frajka-Williams, E. F., Desbruyères, D. G., Beaulie, C., Johns, W. E., et al. (2020). Pending recovery in the strength of the meridional overturning circulation at 26°N. *Ocean Science*, *16*, 863–874. https://doi.org/10.5194/os-16-863-2020

Molinari, R. L., Bauer, S., Snowden, D., Johnson, G. C., Bourlès, B., Gouriou, Y., & Mercier, H. (2003). A comparison of kinematic evidence for tropical cells in the Atlantic and Pacific oceans. *Interhemispheric Water Exchange in the Atlantic Ocean* (Vol. 68, pp. 269–286). Elsevier Oceanography Series. https://doi.org/10.1016/S0422-9894(03)80150-2

Perez, R. C., Hormann, V., Lumpkin, R., Brandt, P., Johns, W. E., Hernandez, F., et al. (2014). Mean meridional currents in the central and eastern equatorial Atlantic. *Climate Dynamics*, *43*(11), 2943–2962. https://doi.org/10.1007/s00382-013-1968-5

Rabe, B., Schott, F. A., & Köhl, A. (2008). Mean Circulation and Variability of the Tropical Atlantic during 1952-2001 in the GECCO Assimilation fields. *Journal of Physical Oceanography*, *38*(1), 177–192. https://doi.org/10.1175/2007JPO3541.1

Rahmstorf, S. (2002). Ocean circulation and climate during the past 120,000 years. *Nature*, *419*, 207–214. https://doi.org/10.1038/nature01090

Ricciardulli, L., & Wentz, F. J. (2016). *Remote sensing systems ASCAT C-2015 daily ocean vector winds on 0.25 deg grid, version 02.1: Remote sensing systems*. Retrieved from www.remss.com/missions/ascat

Roemmich, D. (1983). The balance of geostrophic and Ekman transports in the tropical Atlantic ocean. *Journal of Physical Oceanography*, *13*(8), 15342–1539. https://doi.org/10.1175/1520-0485(1983)013<1534:tbogae>2.0.co;2

Roemmich, D., & Gilson, J. (2009). The 2004–2008 mean and annual cycle of temperature, salinity, and steric height in the global ocean from the Argo Program. *Progress in Oceanography*, *82*(2), 81–100. https://doi.org/10.1016/j.pocean.2009.03.004

Rühs, S., Schwarzkopf, F. U., Speich, S., & Biastoch, A. (2019). Cold vs. warm water route–Sources for the upper limb of the Atlantic meridional overturning circulation revisited in a high-resolution ocean model. *Ocean Science*, *15*, 489–512. https://doi.org/10.5194/os-15-489-2019

Send, U., Lankhorst, M., & Kanzow, T. (2011). Observation of decadal change in the Atlantic meridional overturning circulation using 10 years of continuous transport data. *Geophysical Research Letters*, *38*, L24606. https://doi.org/10.1029/2011GL049801

Schott, F. A., Brandt, P., Hamann, M., Fischer, J., & Stramma, L. (2002). On the boundary flow off Brazil at 5–10°S and its connection to the interior tropical Atlantic. *Geophysical Research Letters*, *29*(17), 1840. https://doi.org/10.1029/2002GL014786

Schott, F. A., Dengler, M., Brandt, P., Affler, K., Fischer, J., Bourlès, B., et al. (2003). The zonal currents and transports at 35°W in the tropical Atlantic. *Geophysical Research Letters*, *30*(7), 1349. https://doi.org/10.1029/2002GL016849

Schott, F. A., Dengler, M., Zantopp, R., Stramma, L., Fischer, J., & Brandt, P. (2005). The shallow and deep western boundary circulation of the South Atlantic at 5°–11°S. *Journal of Physical Oceanography*, *35*(11), 2031–2053. https://doi.org/10.1175/JPO2813.1

Schott, F. A., Fischer, J., & Stramma, L. (1998). Transports and pathways of the upper-layer circulation in the Western Tropical Atlantic. *Journal of Physical Oceanography*, *28*(10), 19042–1928. https://doi.org/10.1175/1520-0485(1998)028<1904:tapotu>2.0.co;2

Schott, F. A., McCreary, J. P., & Johnson, G. C. (2004). Shallow overturning circulations of the tropical-subtropical oceans. *Earth Climate: The Ocean-Atmosphere Interaction. Geophysical Monography Series*, *147*, 261–304. https://doi.org/10.1029/147GM15

Speich, S., Blanke, B., & Madec, G. (2001). Warm and cold water routes of an O.G.C.M. thermohaline Conveyor Belt. *Geophysical Research Letters*, *28*(2), 311–314. https://doi.org/10.1029/2000GL011748

Stramma, L., & England, M. (1999). On the water masses and mean circulation of the South Atlantic Ocean. *Journal of Geophysical Research*, *104*(C9), 20863–20883. https://doi.org/10.1029/1999JC900139

Stramma, L., Fischer, J., & Reppin, J. (1995). The North Brazil undercurrent. *Deep-Sea Research Part I: Oceanographic Research Papers*, *42*, 773–795. https://doi.org/10.1016/0967-0637(95)00014-W

Stramma, L., & Schott, F. A. (1999). The mean flow field of the tropical Atlantic Ocean. *Deep-Sea Research Part II: Topical Studies in Oceanography*, *46*, 279–303. https://doi.org/10.1016/S0967-0645(98)00109-X

Toole, J. M., Andres, M., Le Bras, I. A., Joyce, T. M., & McCartney, M. S. (2017). Moored observations of the Deep Western Boundary Current in the NW Atlantic: 2004–2014. *Journal of Geophysical Research: Oceans*, *122*, 7488–7505. https://doi.org/10.1002/2017JC012984

Tuchen, F. P., Brandt, P., Lübbecke, J. F., & Hummels, R. (2022). Mean current velocity sections along 11°S, 5°S, 35°W, and 23°W from shipboard measurements used in "Transports and pathways of the tropical AMOC return flow from Argo data and shipboard velocity measurements" (Version 1). [Data set], Zenodo. https://doi.org/10.5281/zenodo.5772272

Tuchen, F. P., Lübbecke, J. F., Brandt, P., & Fu, Y. (2020). Observed transport variability of the Atlantic subtropical cells and their connection to tropical sea surface temperature variability. *Journal of Geophysical Research: Oceans*, *125*, e2020JC016592. https://doi.org/10.1029/2020JC016592

Tuchen, F. P., Lübbecke, J. F., Schmidtko, S., Hummels, R., & Böning, C. W. (2019). The Atlantic subtropical cells inferred from observations. *Journal of Geophysical Research: Oceans*, *124*, 7591–7605. https://doi.org/10.1029/2019JC015396

Wilson, W. D., & Johns, W. E. (1997). Velocity structure and transports in the Windward Islands passage. *Deep-Sea Research I*, *44*(3), 487–520. https://doi.org/10.1016/S0967-0637(96)00113-6

Wong, A. P. S., Wijffels, S. E., Riser, S. C., Pouliquen, S., Hosoda, S., Roemmich, D., et al. (2020). Argo data 1999–2019: Two million temperature-salinity profiles and subsurface velocity observations from a global array of profiling floats. *Frontiers in Marine Science*, *7*. https://doi.org/10.3389/fmars.2020.00700

Worthington, E. L., Moat, B. I., Smeed, D. A., Mecking, J. V., Marsh, R., & McCarthy, G. D. (2021). A 30-year reconstruction of the Atlantic meridional overturning circulation shows no decline. *Ocean Science*, *17*, 285–299. https://doi.org/10.5194/os-17-285-2021

Zhang, D., McPhaden, M. J., & Johns, W. E. (2003). Observational evidence for flow between the subtropical and tropical atlantic: The atlantic subtropical cells. *Journal of Physical Oceanography*, *33*(8), 1783–1797. https://doi.org/10.1175/2408.1

Zhang, R., & Thomas, M. (2021). Horizontal circulation across density surfaces contributes substantially to the long-term mean northern Atlantic Meridional Overturning Circulation. *Communications Earth & Environment*, *2*, 112. https://doi.org/10.1038/s43247-021-00182-y

Zilberman, N. V., Roemmich, D. H., Gille, S. T., & Gilson, J. (2018). Estimating the velocity and transport of western boundary current systems: A case study of the east Australian current near Brisbane. *Journal of Atmospheric and Oceanic Technology*, *35*(6), 1313–1329. https://doi.org/10.1175/JTECH-D-17-0153.1